Title

Stable Chelation of Zr-89 and Ac-225 with Dual Size-Selective Macrocyclic py2–macrodipa for 225Ac/89Zr Paired Theranostics

Journal

Inorganic Chemistry, 65(28)

ISSN

0020-1669

Authors

Chakraborty, Mou

Lee, Kevin K

Hasson, Abbie

et al.

Publication Date

2026-07-04

DOI

10.1021/acs.inorgchem.6c02206

Stable chelation of Zr-89 and Ac-225 with dual size selective macrocyclic py_2-macrodipa for $^{225}Ac/^{89}Zr$ paired theranostics

Mou Chakraborty[a,b], Kevin K. Lee[c,d], Abbie Hasson[a,b], Thines Kanagasundaram[c], Amanda Fears[a,b], Aohan Hu[c], Justin J. Wilson[c,d], and Daniel L. J. Thorek*[a,b,e]

[a] Department of Radiology, Washington University School of Medicine, St. Louis, Missouri, 63110, USA

[b] Program in Quantitative Molecular Therapeutics, Washington University School of Medicine, St. Louis, Missouri, 63110, USA

[c] Department of Chemistry and Chemical Biology, Cornell University, Ithaca, New York, 14853, USA

[d] Department of Chemistry and Biochemistry, University of California Santa Barbara, Santa Barbara, California, 93106, USA

[e] Department of Biomedical Engineering, Washington University, St. Louis, Missouri, 63110, USA

* Corresponding author

Email Daniel L. J. Thorek
thorekd@wustl.edu

Author ORCID IDs
Mou Chakraborty, 0009-0002-8676-3086
Kevin K Lee, 0000-0002-1510-0237
Abbie Hasson, 0000-0002-3294-0385
Thines Kanagasundaram, 0000-0001-8265-8591
Amanda Fears, 0000-0003-2374-1170
Aohan Hu, 0000-0002-9720-3159
Justin J. Wilson, 0000-0002-4086-7982
Daniel L. J. Thorek, 0000-0003-2437-1239

Abstract

Radiotheranostic agents combine targeted therapeutics and diagnostic imaging, offering more efficient and personalized treatment strategies. Positron emission tomography provides high sensitivity and quantitative accuracy; however, its integration with α-particle radiotherapy remains limited by the lack of chelators capable of stabilizing radionuclides with widely different ionic radii. ^{89}Zr and ^{225}Ac are promising radionuclides for PET imaging and targeted α-therapy, respectively, but require robust and versatile chelation strategies. Herein, we report stable coordination using the 18-membered macrocyclic dual size-selective chelator py_2-macrodipa with $[^{89}Zr]Zr^{4+}$ and $[^{225}Ac]Ac^{3+}$ ions. The chelator demonstrated efficient radiolabeling with both ^{89}Zr and ^{225}Ac, exhibiting ^{89}Zr labeling efficiency comparable to the state-of-the-art chelator DFO at micromolar concentrations. The $[^{89}Zr][Zr(py_2\text{-macrodipa})]^{2+}$ complex showed high stability in human serum and *in vivo*, with minimal uptake in non-specific tissues such as bone and other organs. Similarly, the $[^{225}Ac][Ac(py_2\text{-macrodipa})]^{+}$ complex displayed robust *in vitro* and *in vivo* stability along with a biodistribution clearance profile similar to its ^{89}Zr analog. In addition, a squaramide ethyl ester conjugated bifunctional chelator (py_2-macrodipa-sq) was synthesized for antibody conjugation and assessed using the PD-1 targeting antibody Opdivo. Both ^{89}Zr- and ^{225}Ac-labeled Opdivo-py_2-macrodipa-sq conjugates were obtained with >98% radiochemical purity and demonstrated high stability *in vitro* and *in vivo*. Although the therapeutic construct exhibited higher activity levels in blood and other organs than the diagnostic analog, both cleared over time with similar distribution patterns and low bone uptake. These findings establish py_2-macrodipa and its bifunctional derivative, py_2-macrodipa-sq, as potential chelation platforms for the development of matched ^{89}Zr/^{225}Ac radiotheranostic agents, demonstrating stable and comparable *in vivo* behavior.

Introduction

Radiotheranostics are an innovative approach in the precision medicine landscape in that they fuse diagnostic and therapeutic capabilities for pre-treatment planning, real-time dosimetry, and monitoring of treatment response. Together this offers improved and personalized targeted treatments while minimizing off-target toxicity [1,2]. For optimal application, quantitative assessment of the distribution of therapeutic radioisotopes is important to assist in absorbed dose measures and monitoring response over cycles of treatment. However, limitations in the quantitative accuracy, sensitivity, and resolution of single photon emission computed tomography (SPECT) imaging when using therapeutic emitters are a challenge [3,4]. Inaccuracies are exacerbated at the ultralow activity levels involved in targeted alpha particle (α) emitting therapies [5–7]. Positron emission tomography (PET) offers superior sensitivity, quantitative precision and resolution over SPECT [8,9]; however, there are no readily available positron emitting therapeutic isotopes. Modification between therapeutic and diagnostic analogs of the same agent ideally involves the single atom substitution of a positron emitter for a therapeutic radionuclide. Use of radiometals requires their stable chelation with the targeting vector (antibody or peptide) that remains intact *in vivo*. However, a fundamental challenge is to ensure that chemical changes to the theranostics have minimal impact on pharmacokinetic behavior, and there are few stable and effective chelators that can conjugate both positron emitting-diagnostic and therapeutic isotopes to a targeting molecule without compromising function.

Instability of the metal-chelate system can lead to premature release of isotopes, reducing effectiveness, and potentially increasing toxicity. This study adopts a dual approach that combines detailed coordination chemistry investigations of radiometal-chelator with *in vivo* radiochemical evaluation, to assess the translational relevance of these systems under biological conditions. While coordination chemistry provides key information on metal-ligand affinity, thermodynamic stability, and coordination geometry, the chemical speciation and stability of radiometal complexes *in vivo* may differ substantially due to the complexity of the physiological environment. We focused on Zirconium-89 (^{89}Zr), a promising candidate for pre- and clinical diagnostic PET imaging [10,11] due to its favorable half-life (t1/2 = 78.4 h), which is well matched with the pharmacokinetics of monoclonal antibodies [12,13], enabling high-resolution and quantitative assessment of their *in vivo* distribution. In addition, ^{89}Zr has been successfully incorporated into peptide-based radiopharmaceuticals, enabling delayed imaging [14–16]. The radionuclide pair Zr-89 and Actinium-225 (^{225}Ac) represents a promising theranostic combination due to their compatible half-lives. Prior studies have highlighted the potential of this combination for

coordinated imaging and targeted alpha therapy [17–19]. Desferrioxamine (DFO, **Figure 1**) remains the most commonly used chelator for ^{89}Zr, particularly for antibody conjugation [20,21]; however, DFO is unsuitable for α-emitting radiometals with expanded ionic radii such as Actinium-225 (^{225}Ac), Thorium-227 (^{227}Th), and Radium-223 (^{223}Ra). The development of a single chelator capable of stably coordinating both diagnostic ^{89}Zr and therapeutic α-emitters would therefore significantly advance radiotheranostic applications.

DOTA (1,4,7,10-Tetraazacyclododecane-N,N',N'',N'''-tetraacetic acid) is the most widely used macrocyclic chelator in radiopharmaceuticals due to its ability to form stable complexes with diverse radionuclides. Recent findings have shown that tetraazamacrocyclic DOTA may be superior chelator for ^{89}Zr compared to DFO, demonstrating high *in vitro* and *in vivo* stability [22], yet this requires heat and time to encourage thermodynamically stable complexes with low charge density, large-radius metal ions, limiting use for protein labeling [23,24]. Recently, we identified the 18-membered macrocyclic chelator macropa, which shows exceptional affinity for metal ions across a range of ionic radii, and its potential bifunctional derivative for ^{225}Ac has been explored [25]. We have extended that work to ^{223}Ra, the first approved alpha particle emitter [26], demonstrating its utility for large ionic radii, but presenting limited application for radionuclides with smaller ionic radii.

Dual-size selective chelators have emerged as a promising solution. These ligands undergo conformational switching upon metal binding, forming stable complexes with both metal ions of larger ionic radii (10-coordinate, C_2-symmetric conformation A) and smaller ionic radii (8-coordinate, asymmetric conformation B). Previous investigations demonstrate stable complexation of py-macrodipa ligand with radiometal ions of ionic radii ranging from 1.03 to 0.74 Å, including Lanthanum-135 (^{135}La)), Bismuth-213 (^{213}Bi, ionic radii of 6-coordinated La^{3+} and Bi^{3+} are similar,1.03 Å), which can be used in targeted radionuclide therapy, and a positron emitter Scandium-44 (^{44}Sc,6-coordinated ionic radius of Sc^{3+}:0.74 Å) [27–30]; although its stability with ^{225}Ac is limited. Multiple ionic radii for Ac^{3+} have been reported in the literature. Zachariasen and co-workers determined a value of 1.11 Å for six-coordinate Ac^{3+} [31–33], which is consistent with Shannon's estimate of 1.12 Å [30]. More recently, Lundberg and Persson proposed a larger ionic radius of 1.220 Å for Ac^{3+} with a coordination number of nine [34]. The relatively large ionic size and diffuse charge of this ion contribute to weaker metal-ligand interactions. The third-generation ligand py_2-macrodipa demonstrates improved thermodynamic and kinetic stability with ^{225}Ac [35]. We have expanded this work towards diagnostic SPECT imaging radionuclide Indium-111 (^{111}In) with small ionic radius[36].

In light of these advancements, we investigated further application of the py_2-macrodipa for radiotheranostics. The six-coordinate and eight-coordinate ionic radii of Zr^{4+} are 0.72 Å and 0.84 Å, respectively, which are smaller than that of six-coordinate and eight-coordinate In^{3+} (0.80 Å and 0.92 Å respectively) [30]. For stable and effective chelation, the size of the metal ion should ideally match the spatial arrangement and distance between the donor atoms. Moreover, Zr(IV), a tetravalent and strongly oxophilic metal ion with a relatively small ionic radius, exhibits a pronounced preference for hydroxo and other oxygen-donor ligands, consistent with its hard Lewis acid character and high affinity for oxygen. Consequently, chelating Zr^{4+} with 18-membered macrocyclic chelator py_2-macrodipa would be expected to be challenging. Yet surprisingly we demonstrate successful coordination of this ligand with Zr^{4+}, optimal labeling conditions, and assessed its suitability for both ^{89}Zr and ^{225}Ac through *in vitro* and *in vivo* studies. To further evaluate the *in vivo* relevance of this chelator, we developed a squaramide ethyl ester conjugated chelator, py_2-macrodipa-sq. Unlike isothiocyanates, squaramide ethyl esters are highly resistant to hydrolysis and offer extended shelf stability [37–39]. We investigated its performance when py_2-macrodipa-sq conjugated to the FDA-approved anti-PD-1 antibody Opdivo (Nivolumab). Antibody-chelator conjugates were efficiently radiolabeled with both ^{89}Zr and ^{225}Ac and assessed for stability and *in vivo* performance. These studies establish py_2-macrodipa as a versatile platform capable of supporting matched immuno-PET imaging and targeted alpha therapy using a single antibody construct.

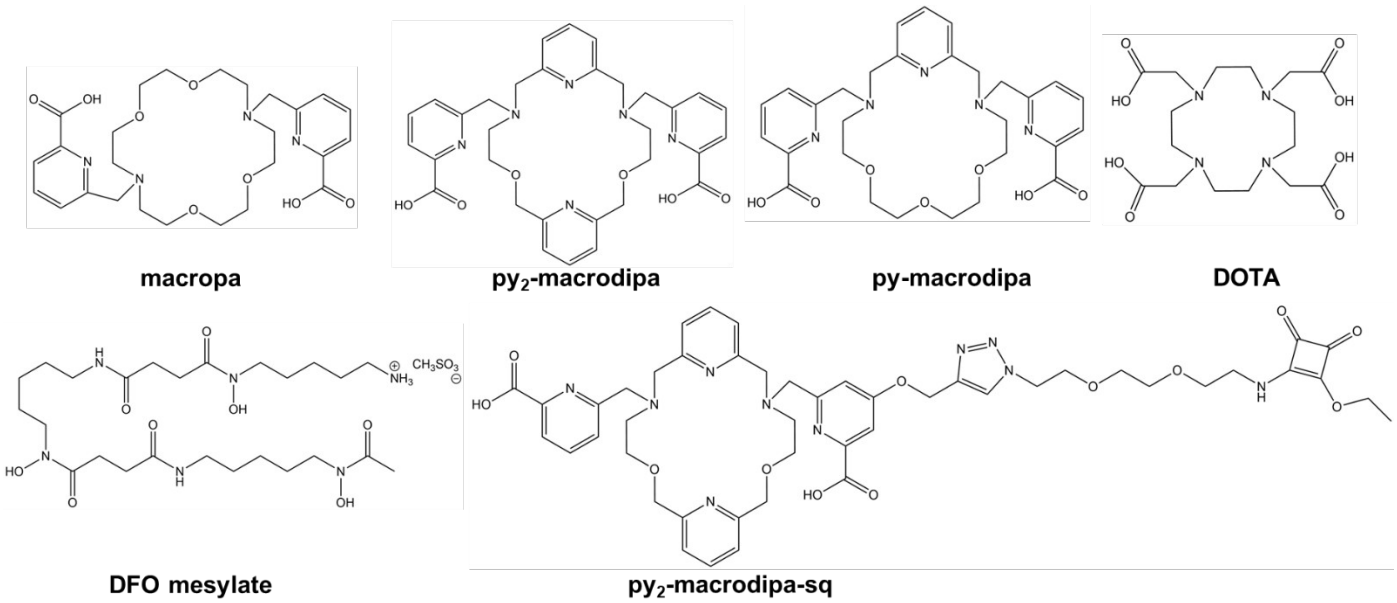

Figure 1. Structures of the ligands discussed in this work.

Results

$[Zr(py_2\text{-macrodip})]^{2+}$ Complex Characterization

To evaluate the potential of py_2-macrodipa for ^{89}Zr PET imaging, the $[Zr(py_2\text{-macrodipa})]^{2+}$ complex was characterized by ^1H NMR spectroscopy. NMR sample was prepared by incubating aqueous solution of py_2-macrodipa· and $Zr(acac)_4$ (1:1 metal:ligand ratiol). The pH of the solution was adjusted to 5.0 using 1 M NaOH, and the mixture was stirred at room temperature overnight. The resulting product was isolated by lyophilization as a white solid and used directly for subsequent ^1H NMR analysis. Previous studies have shown that ligands similar to py_2-macrodipa form complexes with distinct geometries depending on the preferred coordination environment of the metal ion, with metal ions favoring higher coordination numbers (e.g., La^{3+}) adopting a symmetric Conformation A, whereas those favoring lower coordination numbers (e.g., In^{3+}) adopt an asymmetric Conformation B (**Figure 2**). The ^1H NMR spectrum of $[Zr(py_2\text{-macrodipa})]^{2+}$ displayed well-resolved aromatic resonances and split aliphatic signals, including two distinct sets of picolinate resonances, indicating an asymmetric coordination environment. Comparison with La^{3+} and In^{3+} complexes (**Figure 3**) revealed that the Zr^{4+} spectrum closely resembles that of In^{3+} in terms of the number of resonances and chemical shifts, strongly suggest that Zr^{4+} adopts the asymmetric Conformation B.

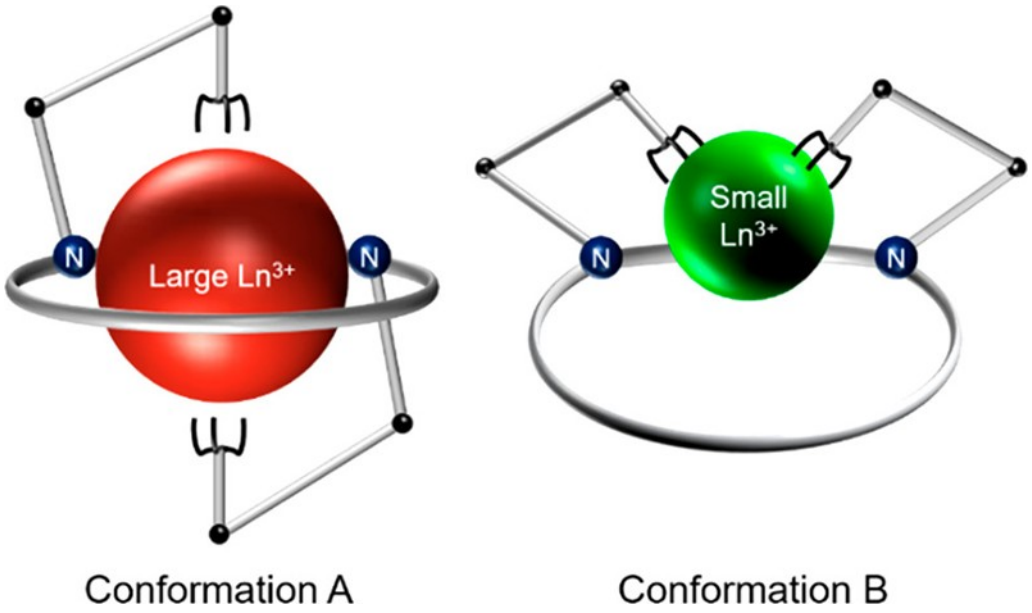

Figure 2. Depiction of the conformational switch present in Ln^{3+}-py_2-macrodipa complex. Reproduced with permission from A. Hu, S. N. MacMillan, J. J. Wilson. Macrocyclic ligands with an unprecedented size-selectivity pattern for the lanthanide ions. J Am Chem Soc. 2020; 142: 13500-13506. Copyright 2020 American Chemical Society.

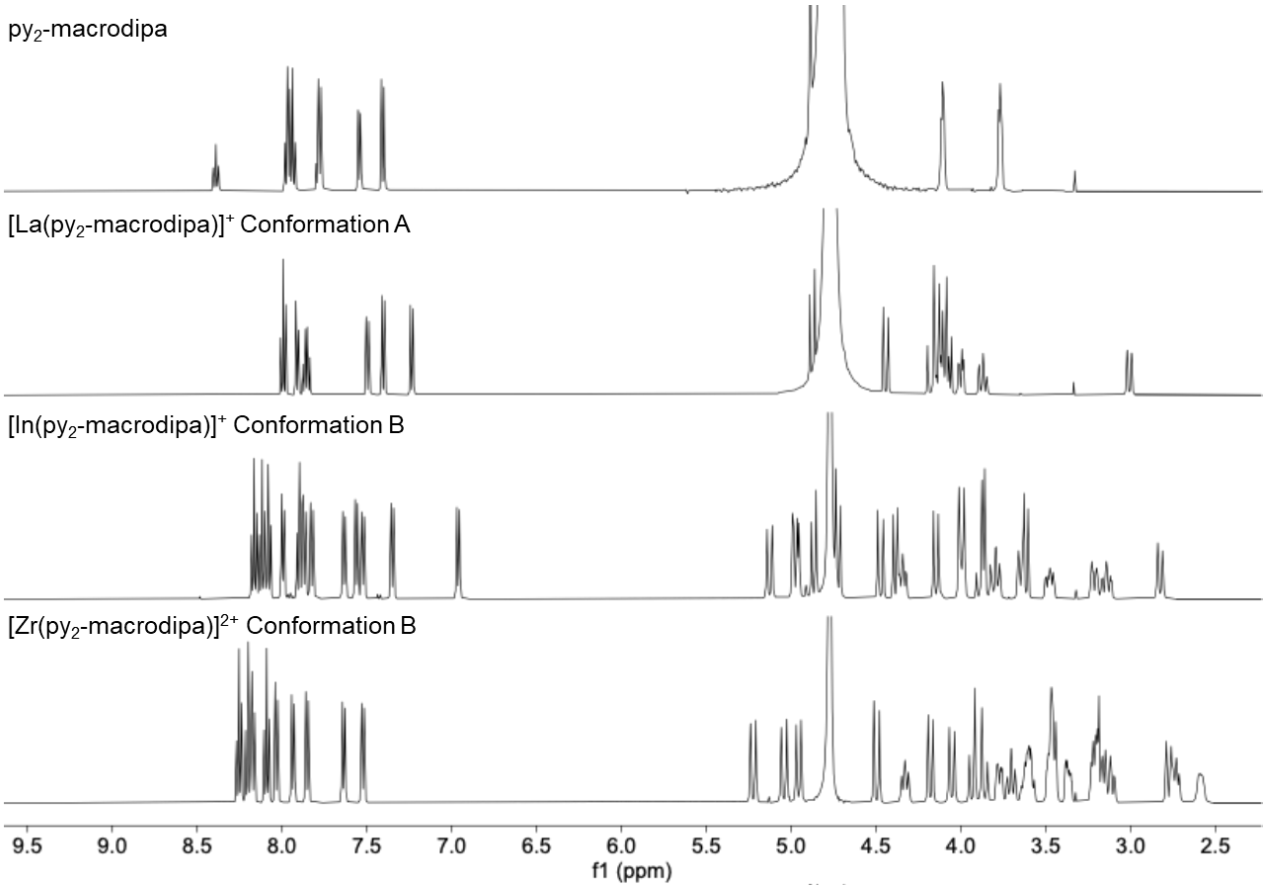

Figure 3. ^{1}H NMR spectra of py_2-macrodipa, $[La(py_2\text{-macrodipa})]^{+}$, $[In(py_2\text{-macrodipa})]^{+}$, and $[Zr(py_2\text{-macrodipa})]^{2+}$ (500 MHz, D_2O, pD 5, 25 °C). The Zr^{4+} spectrum closely resembles that of In^{3+} strongly suggesting that Zr^{4+} adopts the asymmetric Conformation B.

Although we were unable to obtain crystals of the py_2-macrodipa complex, we successfully grew suitable crystals of the Zr complex with the second-generation dual-size selective ligand py-macrodipa (**Figure 4**). The ^{1}H NMR spectra of these crystals clearly indicate the presence of Conformation B in the chelator arrangement as shown in **Figure S1**. The solid-state structure of $[Zr(py\text{-}macrodipa)(OMe)]^{+}$ reveals an 8-coordinate Zr(IV) center with an N_5O_3 donor set. The coordination sphere is composed of the pyridyl nitrogen donors, two tertiary amine donors of the macrocycle, two picolinate oxygen atoms, and an inner-sphere methoxide ligand. The Zr–O bond distances span 1.94-2.18 Å**,** while the Zr–N bond distances range from 2.33 to 2.51 Å, consistent with strong coordination to oxygen donors and slightly longer interactions with nitrogen donors. The coordination geometry can be described as a distorted eight-coordinate polyhedron, deviating from an ideal square-antiprismatic arrangement due to the constrained topology of the macrocycle and the asymmetric donor distribution associated with Conformation B. In contrast to the previously reported $[In(py\text{-}macrodipa)]^{+}$ structure [33], in which the eighth coordination site is occupied by the macrocyclic ether oxygen, the [Zr(py-macrodipa)

(OMe)]$^{+}$ structure adopts a different coordination mode in which the ether oxygen is not bound, and a methoxide ligand completes the coordination sphere. The presence of this inner-sphere methoxide results in a more expanded macrocyclic conformation. Similar coordination of solvent-derived ligands has been observed in related [In(py$_2$-macrodipa)(OH$_2$)]$^{+}$ complex, where inner-sphere water molecule was present. These observations suggest a degree of structural flexibility, in which exchange between an inner-sphere solvent molecule and the macrocyclic ether donor may occur. Accordingly, slight variations in crystallization conditions may favor the isolation of distinct coordination modes. The identity of the complex is further supported by ESI-HRMS (**Figure S2**).

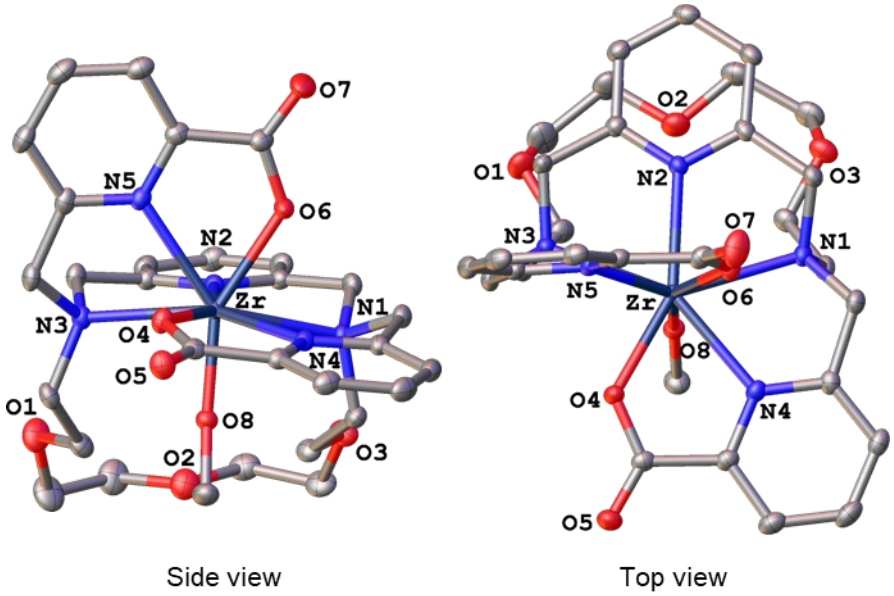

Figure 4. Crystal structure of. [Zr(py-macrodipa)OMe][Cl]DMF. Thermal ellipsoids are drawn at the 50% probability level. Solvent, counterions, and non-acidic hydrogen atoms are omitted for clarity.

Radiolabeling with Zr-89

To investigate the potential for chelation with macropa and py$_2$-macrodipa towards [^{89}Zr]Zr^{4+}, concentration-dependent radiolabeling studies were performed and compared with control DFO-complex. Ligands were incubated with 0.2 MBq of [^{89}Zr]Zr^{4+} (in oxalic acid) in pH 6.5 HEPES buffer, and radiochemical yields (RCYs) were assessed by radio-TLC (iTLC-SG; **Figure 5**). Notably, py$_2$-macrodipa quantitatively incorporates [^{89}Zr]Zr^{4+} at a low concentration of 10^{-6} M at 90°C within 30 min achieving an RCY of 87% (**Figure 6**, **Table S1**). Following C18 cartridge purification, a radiochemical purity of 97% was obtained (**Figure S12**). These results are comparable to DFO, which quantitatively complexes [^{89}Zr]Zr^{4+} at micromolar concentrations with RCY >97% at 37 °C, highlighting

that both ligands can be efficiently radiolabeled at micromolar concentrations, although py_2-macrodipa requires a higher reaction temperature. Radiolabeling of py_2-macrodipa at 37 °C afforded moderate RCYs (35-40%), By contrast, quantitative radiolabeling of DOTA with $[^{89}Zr]Zr^{4+}$ typically requires elevated temperature conditions ~90 °C. Whereas efficient radiolabeling of macropa was observed at relatively high ligand concentrations (15 mM), as confirmed by TLC analysis and concentration-dependent studies. At lower concentrations, the radiolabeling efficiency decreased significantly (**Figure 6**). Extending the reaction time to 60 min did not improve RCYs.

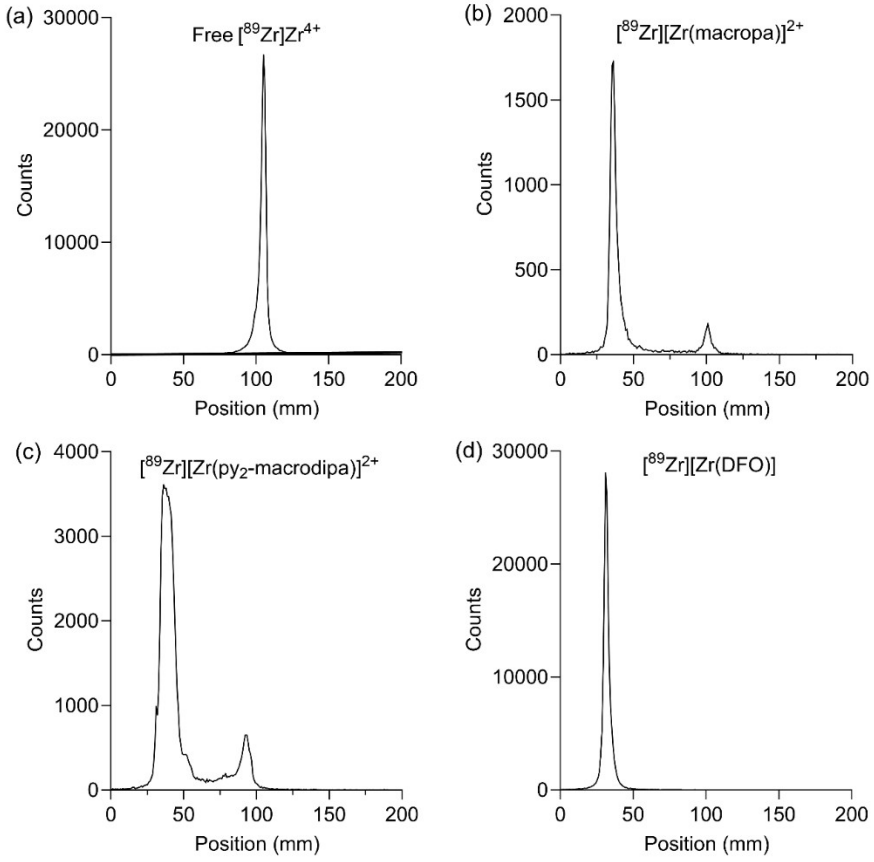

Figure 5. Thin-layer chromatograms of free (a) $[^{89}Zr]Zr^{4+}$, (b) $[^{89}Zr][Zr(macropa)]^{2+}$, (c) $[^{89}Zr][Zr(py_2\text{-macrodipa})]^{2+}$ and (d) $[^{89}Zr][Zr(DFO)]$; iTLC-SG eluted with 50 mM EDTA pH 5.5; free $[^{89}Zr]Zr^{4+}$ migrated with the solvent front (R_f = 1), whereas the complex species remained at the baseline (R_f = 0); ligand concentration used 15 × 10^{-3} M; activity of ^{89}Zr source 0.2MBq; 90 ˚C for (a), (b) and (c);37 ˚C for (d); 30 min.

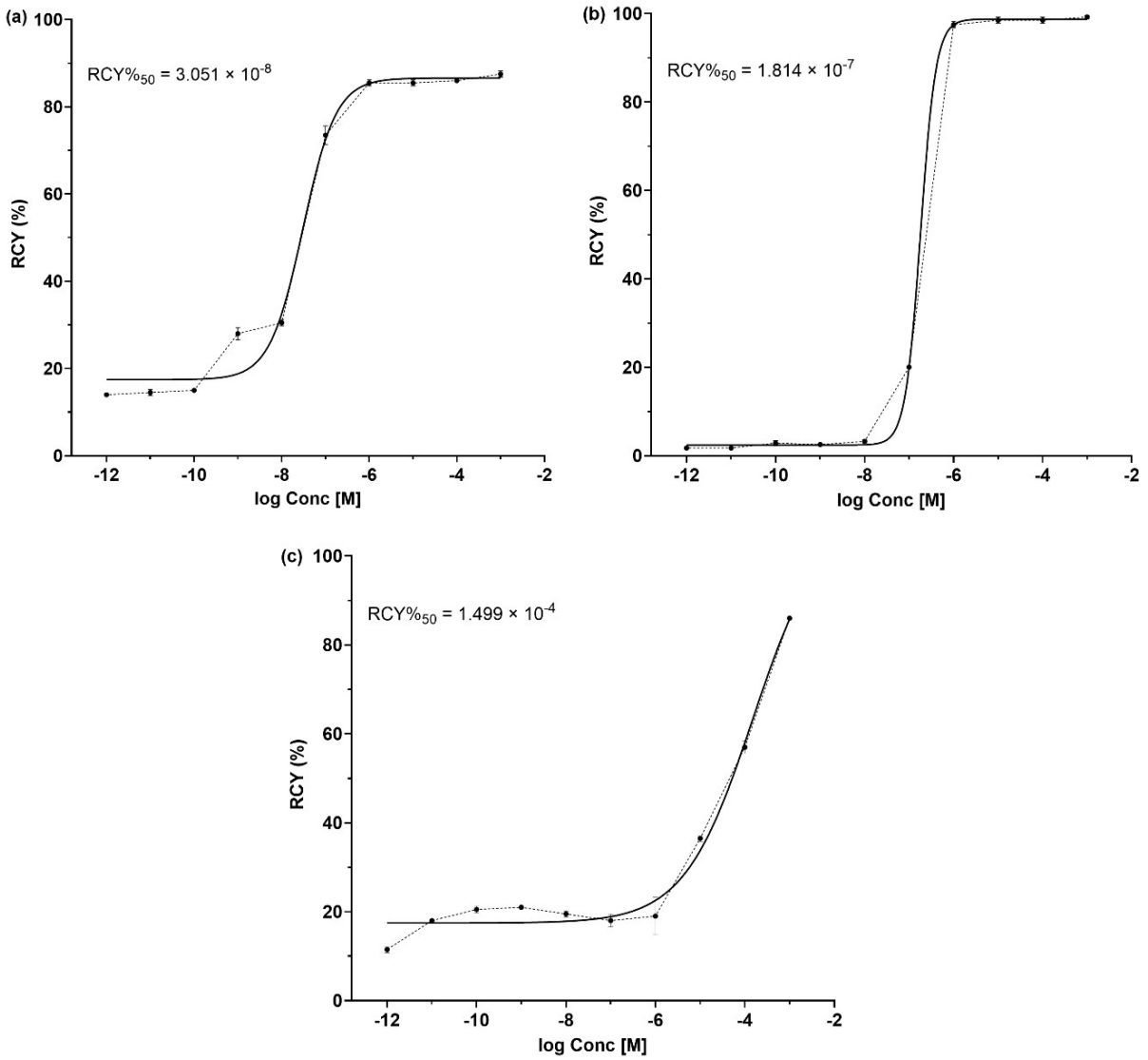

Figure 6. Radiochemical yields% (RCY%) of ^{89}Zr radiolabeling with (a) py$_2$-macrodipa, (b) DFO and (c) macropa at different ligand concentrations; the ligand concentration required for 50% RCY% (RCY%$_{50}$) for py$_2$-macrodipa, DFO and macropa were found to be 3.051 $\times 10^{-8}$, 1.814 $\times$ 10^{-7}.and 1.499 $\times$ 10^{-4} M respectively.

Radiolabeling studies were also conducted using [^{89}Zr]ZrCl$_4$ to assess potential differences in chelation behavior. Concentration-dependent experiments (micromolar to millimolar) were performed with ~1.85 MBq of [^{89}Zr]ZrCl$_4$ in pH 6.5 HEPES buffer at 25 °C for 1 h. As illustrated in **Figure S13a**, DFO achieved nearly 100% radiochemical conversion, while DOTA, macropa and py$_2$-macrodipa failed to incorporate [^{89}Zr]ZrCl$_4$

under these conditions (**Figure S14**, **Table S2**). At 90 °C, as expected, DOTA exhibited nearly complete conversion, while DFO failed to label due to limited thermal stability (**Figure S13b**). Notably, macropa and py_2-macrodipa also failed to incorporate $[^{89}Zr]Zr^{4+}$ under these conditions (**Figure S15**, **Table S3**), in contrast to their behavior with $[^{89}Zr]Zr^{4+}$ in oxalic acid. This selective radiolabeling of py_2-macrodipa with oxalate-derived $[^{89}Zr]Zr^{4+}$ may offer advantages for the development of ^{89}Zr-based PET radiotracers.

Radiolabeling with Ac-225

Having established the successful radiolabeling with the $[^{89}Zr]Zr^{4+}$ ion (in oxalic acid), we subsequently evaluated $[^{225}Ac]Ac^{3+}$ to evaluate *in vivo* stability and potential as a candidate for targeted α therapy (TAT). Both macropa and py_2-macrodipa were efficiently radiolabeled with $[^{225}Ac]Ac^{3+}$ in 0.5 M ammonium acetate buffer (pH 6.0) at room temperature, achieving high radiochemical yields (95-98%) within 5 min under mild conditions (**Figure 7**). These results demonstrate the favorable radiolabeling properties of py_2-macrodipa, enabling effective coordination of both metal ions with higher charge density,such as $[^{89}Zr]Zr^{4+}$, as well as those with lower charge density $[^{225}Ac]Ac^{3+}$ ion.

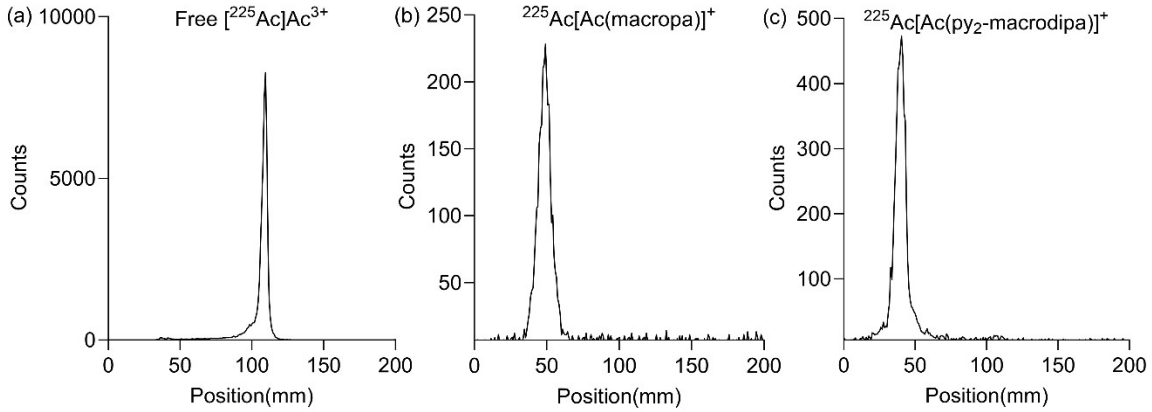

Figure 7. Thin-layer chromatograms of free (a) $[^{225}Ac]Ac^{3+}$, (b) $[^{225}Ac][Ac(macropa)]^{+}$ and (c) $[^{225}Ac][Ac(py_2\text{-macrodipa})]^{+}$, iTLC-SG eluted with 50mM EDTA pH5.5; free $[^{225}Ac]Ac^{3+}$ migrated with the solvent front (R_f = 1), whereas the complex species remained at the baseline (R_f ~ 0).

***In Vitro* Stability**

Kinetic stability in human serum was evaluated to assess the stability of these complexes under physiological conditions. The ^{89}Zr-complexes of py_2-macrodipa, macropa, and DFO were incubated in human serum at 37 °C for up to 48 h and analyzed by radio-TLC (**Figure S17**). $[^{89}Zr][Zr(py_2\text{-macrodipa})]^{2+}$ showed high stability, with >96% remaining

intact after 48 h, comparable to DFO (**Figure 8**, **Table S4**). In contrast, only 48% of [^{89}Zr][Zr(macropa)]$^{2+}$ remained intact after 24 h. Although the formation of the [^{89}Zr][Zr(macropa)]$^{2+}$ complex was confirmed by early timepoint radio-TLC, the complex exhibited limited *in vitro* stability, as revealed by its behavior in human serum during later time point analysis. The kinetic inertness to serum of [^{225}Ac][Ac(macropa)]$^{+}$ and [^{225}Ac][Ac(py$_2$-macrodipa)]$^{+}$ is consistent with prior reports (**Figure S16** and **S18**, **Table S5**). Notably, the similarly high stability of the ^{89}Zr and ^{225}Ac-py$_2$-macrodipa complexes supports py$_2$-macrodipa as a promising theranostic chelator for the ^{89}Zr/^{225}Ac pair.

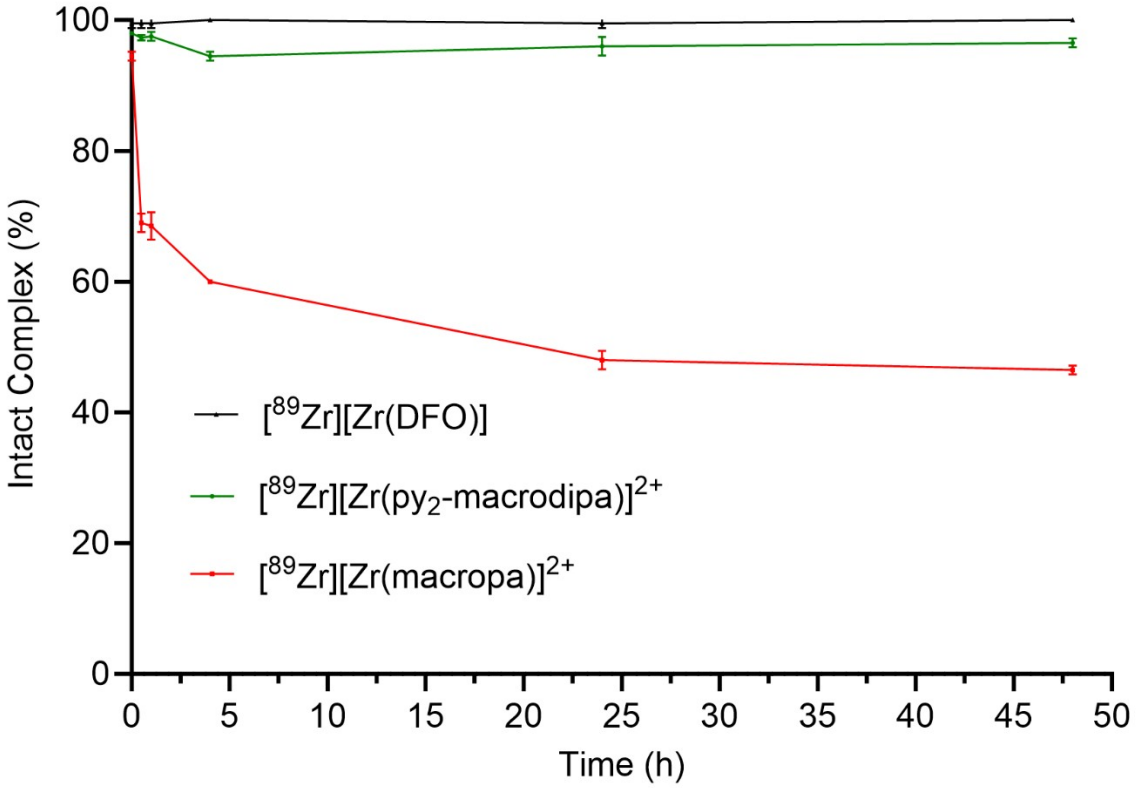

Figure 8. Stability of [^{89}Zr][Zr(DFO)], [^{89}Zr][Zr(py$_2$-macrodipa)]$^{2+}$, [^{89}Zr][Zr(macropa)]$^{2+}$ in human serum over 48h at 37 °C; .as assessed by iTLC, [^{89}Zr][Zr(py$_2$-macrodipa)]$^{2+}$ remained with more than 96% intact, comparable to DFO-complex, whereas [^{89}Zr][Zr(macropa)]$^{2+}$ remained 46% intact after 48h; ligand concentration used 15 × 10^{-3} M.

In Vivo Studies Positron Emission Tomography (PET)

We next investigated *in vivo* stability of the [^{89}Zr][Zr(py$_2$-macrodipa)]$^{2+}$, and [^{89}Zr][Zr(macropa)]$^{2+}$ complexes by PET imaging in naive mice. Projection images and quantitative volumes of interest (VOI) analysis were shown in the SI (**Figure S19** and

Figure S20). At 1 h post injection (p.i), [^{89}Zr][Zr(py$_2$-macrodipa)]$^{2+}$ showed predominant intestinal uptake with minor bladder activity (**Figure 9**); residual gut activity was observed at 4 h and completely cleared by 24 h. Negligible bone uptake at all time points indicated no *in vivo* release of free [^{89}Zr]Zr^{4+} ion. For comparison with the control group, [^{89}Zr][Zr(DFO)] showed only renal excretion, as expected. In contrast, for the [^{89}Zr][Zr(macropa)]$^{2+}$ complex, activity was observed in the bladder at 1-4h p.i. and at 24 h p.i., remaining activity was accumulated in the bone, indicating *in vivo* instability and [^{89}Zr]Zr^{4+} release.

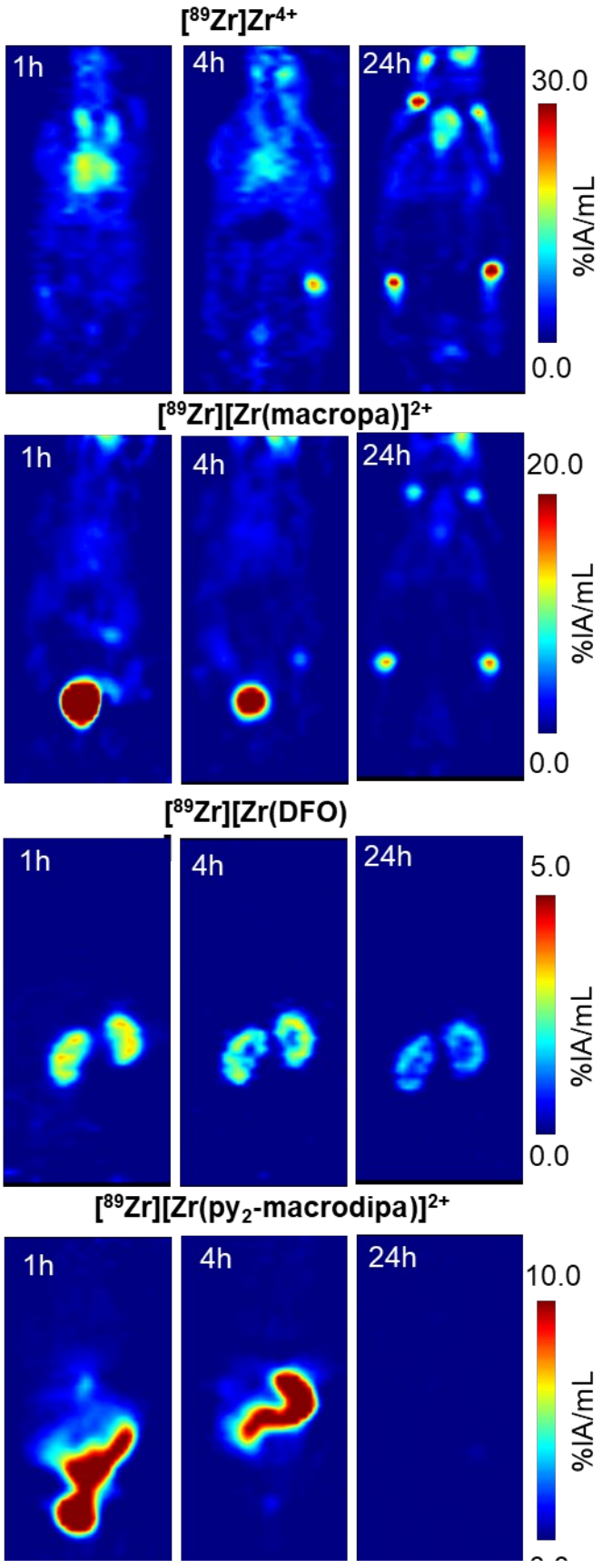
[89Zr]Zr4+
1h
4h
24h
30.0
%IA/mL
0.0
[89Zr][Zr(macropa)]2+
1h
4h
24h
20.0
%IA/mL
0.0
[89Zr][Zr(DFO)
1h
4h
24h
5.0
%IA/mL
0.0
[89Zr][Zr(py2-macrodipa)]2+
1h
4h
24h
10.0
%IA/mL

Figure 9. PET images of representative naive Swiss Webster female mice with $[^{89}Zr]Zr^{4+}$, $[^{89}Zr][Zr(macropa)]^{2+}$, $[^{89}Zr][Zr(DFO)$, and $[^{89}Zr][Zr(py_2\text{-macrodipa})]^{2}$.Free $[^{89}Zr]Zr^{4+}$ was located in the bone at 24h p.i., for $[^{89}Zr][Zr(macropa)]^{2+}$ complex most of the activity accumulated in the bone indicating release of free $[^{89}Zr]Zr^{4+}$ ion, $[^{89}Zr][Zr(DFO)]$ complex was rapidly excreted through the kidneys, whereas $[^{89}Zr][Zr(py_2\text{-macrodipa})]^{2+}$ complex showed gut uptake which was cleared rapidly and no uptake in the bone was observed. Note, the intensity ranges for these coronal sections are fixed across the imaging sessions for each ligand complex, in order to enable visualization of activity distribution.

Biodistribution Studies

Ex vivo biodistribution studies at 1, 4, and 24 h p.i. corroborated the PET findings (**Figure 10**, **Table S8**). The biodistribution profile of free $[^{89}Zr]Zr^{4+}$ revealed slow blood clearance with high bone accumulation (**Figure S21**). $[^{89}Zr][Zr(macropa)]^{2+}$ displayed a similar profile, with blood (4.4 ± 0.4 %IA/g) and kidney activity (3.1 ± 1.1 %IA/g) at 1h p.i. and increasing bone uptake at 24 h (tibia and calvaria with 3.9 ± 0.8 and 8.3 ± 3.4 %IA/g respectively), indicating *in vivo* dissociation and release of $^{89}Zr^{4+}$ (**Figure S24**).

By contrast, the organ distribution profile of $[^{89}Zr][Zr(py_2\text{-macrodipa})]^{2+}$differs significantly from that of free $[^{89}Zr]Zr^{4+}$ It clearly showed rapid intestinal and renal excretion, minimal blood and organ retention, and negligible bone uptake at all time points, consistent with high *in vivo* stability. The majority of the activity localized in the intestine (10.6 ± 15 %IA/g) and kidneys (1.3 ± 0.7 %IA/g) at early time point, was cleared from the body at 24 h p.i.

As expected, $[^{89}Zr][Zr(DFO)]$ was primarily cleared renally with negligible bone accumulation. The biodistribution and clearance profile of $[^{89}Zr][Zr(py_2\text{-macrodipa})]^{2+}$ differs from that of $[^{89}Zr][Zr(DFO)]$ complex with lower tissue retention with the latter ligand, however each ligand was cleared from the organs over time with minimal bone accumulation. The *in vivo* stability of $[^{89}Zr][Zr(py_2\text{-macrodipa})]^{2+}$ indicates potential as a viable candidate for radiopharmaceutical agent development.

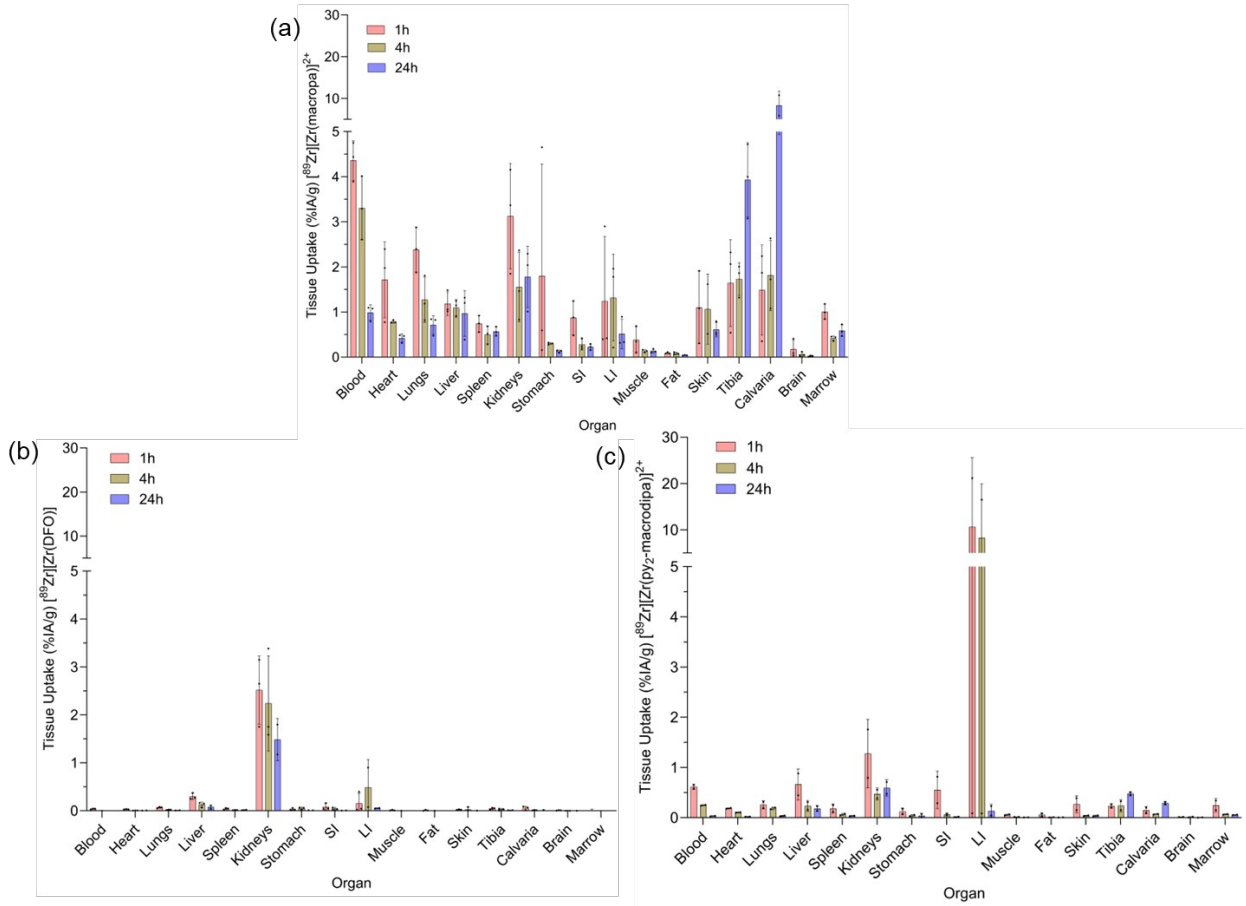

Figure 10. Organ distribution of (a) $[^{89}Zr][Zr(macropa)]^{2+}$, (b) $[^{89}Zr][Zr(DFO)]$ and (c) $[^{89}Zr][Zr(py_2\text{-macrodipa})]^{2+}$ following retro-orbital injection in mice. Naive swiss webster female of 4 months old were sacrificed after 1, 4 and 24h p.i. Values for each time point are given as %IA/g; %IA/g = percent injected activity per g of tissue; SI = small intestine and LI = large intestine. $[^{89}Zr][Zr(macropa)]^{2+}$ showed activity localization in the bone indicating release of free metal ion from the ligand, $[^{89}Zr][Zr(DFO)]$ was rapidly renally excreted, while $[^{89}Zr][Zr(py_2\text{-macrodipa})]^{2+}$ was processed through the intestine and negligible bone uptake at all time points was observed indicating high *in vivo* stability.

Given its efficient radiolabeling and *in vitro* stability with ^{225}Ac, the *in vivo* stability and biodistribution of $[^{225}Ac][Ac(py_2\text{-macrodipa})]^{+}$ were evaluated and compared with $[^{225}Ac][Ac(macropa)]^{+}$ (**Figure 11**). As expected, $[^{225}Ac][Ac(macropa)]^{+}$ showed rapid clearance, with low blood activity at 1 h p.i., predominant renal excretion, and residual intestinal activity at 4 h post administration. $[^{225}Ac][Ac(py_2\text{-macrodipa})]^{+}$ exhibited a similar profile, with low blood retention and rapid clearance, showing kidney, liver and intestinal activity at 4 h p.i. Importantly, negligible activity accumulation was observed in the liver, spleen, or bone, indicating high *in vivo* stability and no release of $[^{225}Ac]Ac^{3+}$.

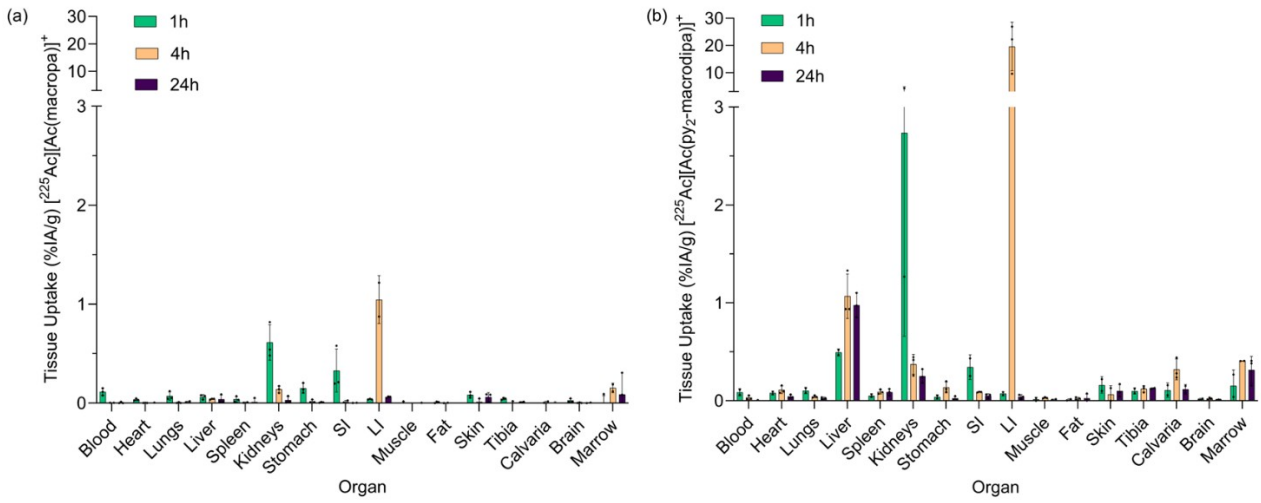

Figure 11. Organ distribution of (a) $[^{225}Ac][Ac(macropa)]^+$ and (b) $[^{225}Ac][Ac(py_{2}\text{-}macrodipa)]^+$ following retro-orbital injection in mice. Naive mice, 4 months old, were sacrificed after 1, 4 and 24h post-administration. Values for each time point are given as %IA/g; %IA/g = percent injected activity per g of tissue; SI = small intestine and LI = large intestine; Both complexes showed rapid intestinal and renal excretion, negligible activity in the bone and other organs over time indicates *in vivo* stability.

A comparison of the biodistribution of $[^{89}Zr][Zr(py_2\text{-macrodipa})]^{2+}$ and $[^{225}Ac][Ac(py_2\text{-macrodipa})]^{+}$ was also conducted. Other than greater measured uptake with the therapeutic analog at the earliest time point of ~1 %IA/g; the salient difference is persistent liver signal. Globally, the distribution profiles reveal intestinal disposal, low uptake in the liver and kidneys and little residual activity in other tissues with time. The distribution and clearance profile are similar, with some differences in activity accumulation was observed at 24 h post injection (**Figure 12b**) of several organs including the liver and bone; $[^{225}Ac][Ac(py_2\text{-macrodipa})]^{+}$ liver uptake (1.0 ± 0.1) was higher than $[^{89}Zr][Zr(py_2\text{-macrodipa})]^{2+}$ (0.2± 0.1) while bone signal (Tibia) was lower (0.1 ± 0.1) than that of $[^{89}Zr][Zr(py_2\text{-macrodipa})]^{2+}$ (0.5 ± 0.04). Comparison of the 4 h and 24 h biodistribution data further indicates substantial clearance of radioactivity over time. Together, these biodistribution studies demonstrate that $[^{89}Zr][Zr(py_2\text{-macrodipa})]^{2+}$ and $[^{225}Ac][Ac(py_2\text{-macrodipa})]^{+}$ are highly stable *in vivo*, an essential attribute to develop $^{225}Ac/^{89}Zr$ paired α/positron radiotheranostic.

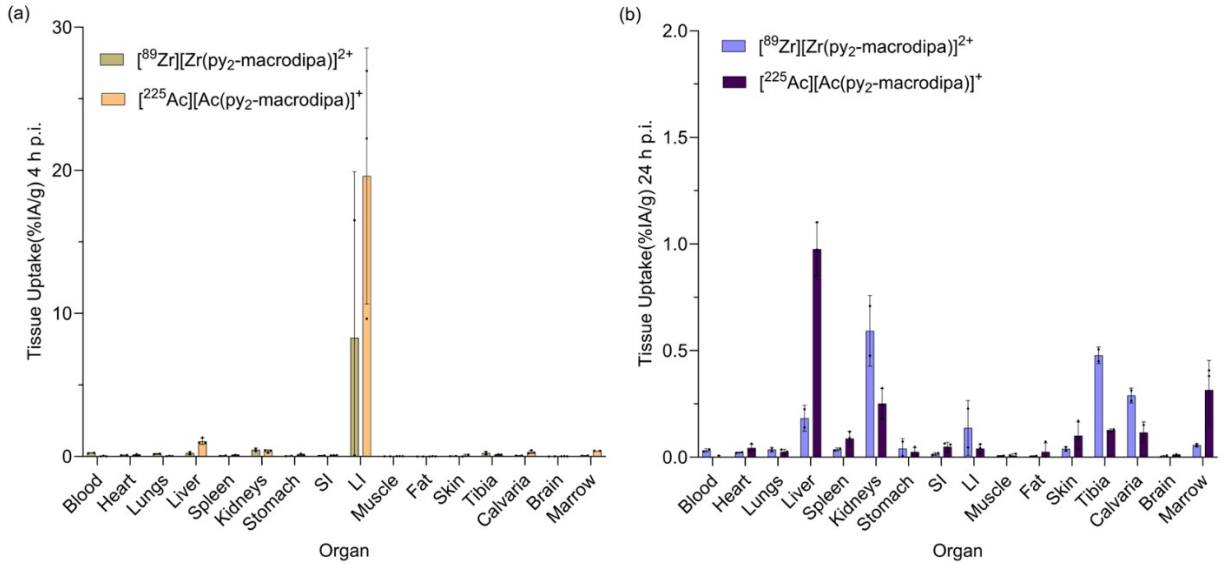

Figure 12. Biodistribution comparison of $[^{89}Zr][Zr(py_2\text{-macrodipa})]^{2+}$ and $[^{225}Ac][Ac(py_2\text{-macrodipa})]^{+}$ complexes at (a) 4 h and (b) 24 h post injection; Values for each time point are given as %IA/g; %IA/g = percent injected activity per g of tissue; SI = small intestine and LI = large intestine; A similar activity distribution profile was observed with activity uptake in the intestine at 4 h ,rapidly excreted at 24 h p.i., negligible activity in the liver, kidneys and bone was observed at 24 p.i. Note, the %IA/g scale was reduced from ~30 at 4 h to ~1.5 at 24 h, reflecting extensive excretion and marked reduction in whole-body radioactivity by the later time point.

Bifunctional chelator py_2-macrodipa-sq

For antibody conjugation, non-symmetric macrocycles with a single, well-defined functionalization site are preferred. However, the synthesis of non-symmetric 4,13-diaza-18-crown-6 ligands is challenging because N-alkylation typically yields mixtures of mono- and disubstituted products. Here, we adapted the reported synthesis of H_2MacropaSqOEt by introducing an alkyne substituent at the 4-position of the picolinate arm to afford compound 6-((10-((6-carboxypyridin-2-yl)methyl)-3,13-dioxa-6,10-diaza-1,8(2,6)-dipyridinacyclotetradecaphane-6-yl)methyl)-4-(prop-2-yn-1-yloxy)picolinic acid (**5**) [40]. Subsequent copper(I)-catalyzed azide-alkyne cycloaddition with an azide-functionalized oligo(ethylene glycol) squaramide ester (3-((2-(2-(2-azidoethoxy)ethoxy)ethyl)amino)-4-ethoxycyclobut-3-ene-1,2-dione **,6**) yielded the bifunctional chelator py_2-macrodipa-sq (6-((10-((6-carboxypyridin-2-yl)methyl)-3,13-dioxa-6,10-diaza-1,8(2,6)-dipyridinacyclotetradecaphane-6-yl)methyl)-4-((1-(2-(2-(2-((2-ethoxy-3,4-dioxocyclobut-1-en-1-yl)amino)ethoxy)ethoxy)ethyl)-1*H*-1,2,3-triazol-4-yl)methoxy)picolinic acid**,**(**7**).

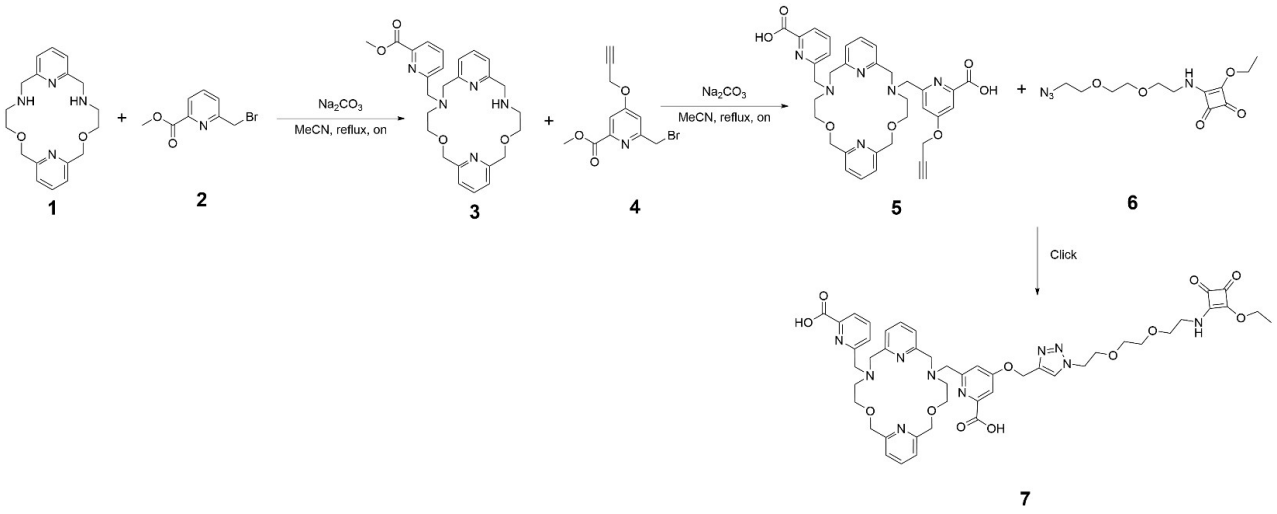

Scheme 1. Synthesis of bifunctional chelator py_2-macrodipa-sq

Antibody conjugation, radiolabeling with Zr-89 and Ac-225 and *in vitro* stability

To evaluate py_2-macrodipa-sq as bifunctional chelator, it was conjugated to the anti-PD-1 antibody Opdivo, in sodium bicarbonate buffer (pH 9.0) overnight at 37 ˚C using 20 equivalents of the chelator. The conjugate was purified from excess unreacted chelator with a spin desalting column which is based on size exclusion chromatography. The conjugate was successfully radiolabeled with ^{89}Zr and ^{225}Ac isotopes, affording radiochemical yields of 80% and 90%, respectively, and >99% radiochemical purity (RCP)

after purification with size exclusion chromatography (**Figure 13a** and **13b**). ^{225}Ac labeled conjugate demonstrated high *in vitro* stability in human serum, with >96% remained intact over 120h (**Figure 13c**, **S22**, **Table S7**). The ^{89}Zr analog maintained ~80% radiochemical stability in human serum over 48 h (**Figure 13c**, **S23,Table S6**).

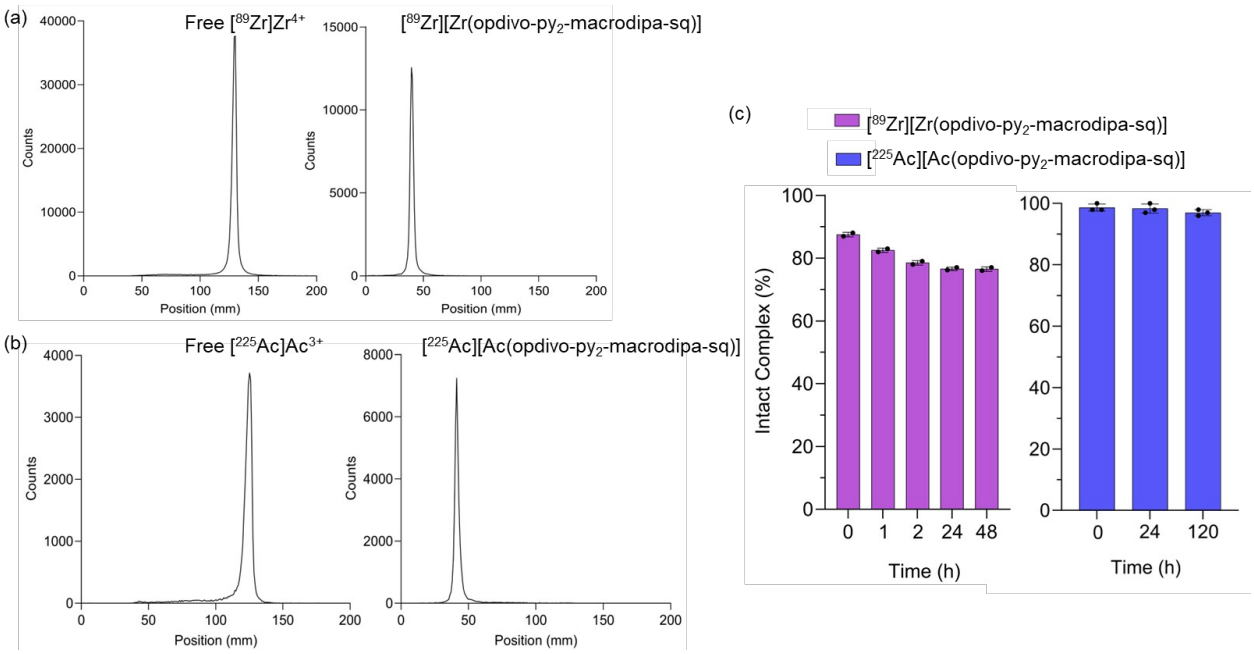

Figure13. Thin-layer chromatograms of free (a) $[^{89}Zr]Zr^{4+}$ and $[^{89}Zr][Zr(opdivo\text{-}py_2\text{-}macrodipa\text{-}sq)]$ (b) $[^{225}Ac]Ac^{3+}$ and $[^{225}Ac][Ac(opdivo\text{-}py_2\text{-}macrodipa\text{-}sq)]^{+}$, iTLC-SG eluted with 50mM EDTA pH5.5; free metals migrated with the solvent front (Rf = 1), whereas the complex species remained at the baseline (Rf ~ 0). (c) Human serum stability over 48h and 120h at 37 °C for ^{89}Zr- and ^{225}Ac-conjugates respectively; as assessed by ITLC, with >96% (for ^{225}Ac conjugate) and ~80% (^{89}Zr-conjugate) radiochemical stability maintained.

PET and Biodistribution Study

The *in vivo* stability of $[^{89}Zr][Zr(opdivo\text{-}py_2\text{-}macrodipa\text{-}sq)]$ was evaluated by PET imaging in naïve mice (**Figure 14**; **Figure S25**). Imaging at 1 p.i. demonstrated predominantly cardiac localization, with moderate liver uptake was observed at 72h. The radioconjugate demonstrated efficient circulation within the blood pool immediately after administration and throughout the imaging period. Importantly, negligible bone uptake was observed at all time points, indicating no *in vivo* release of free $[^{89}Zr]Zr^{4+}$.

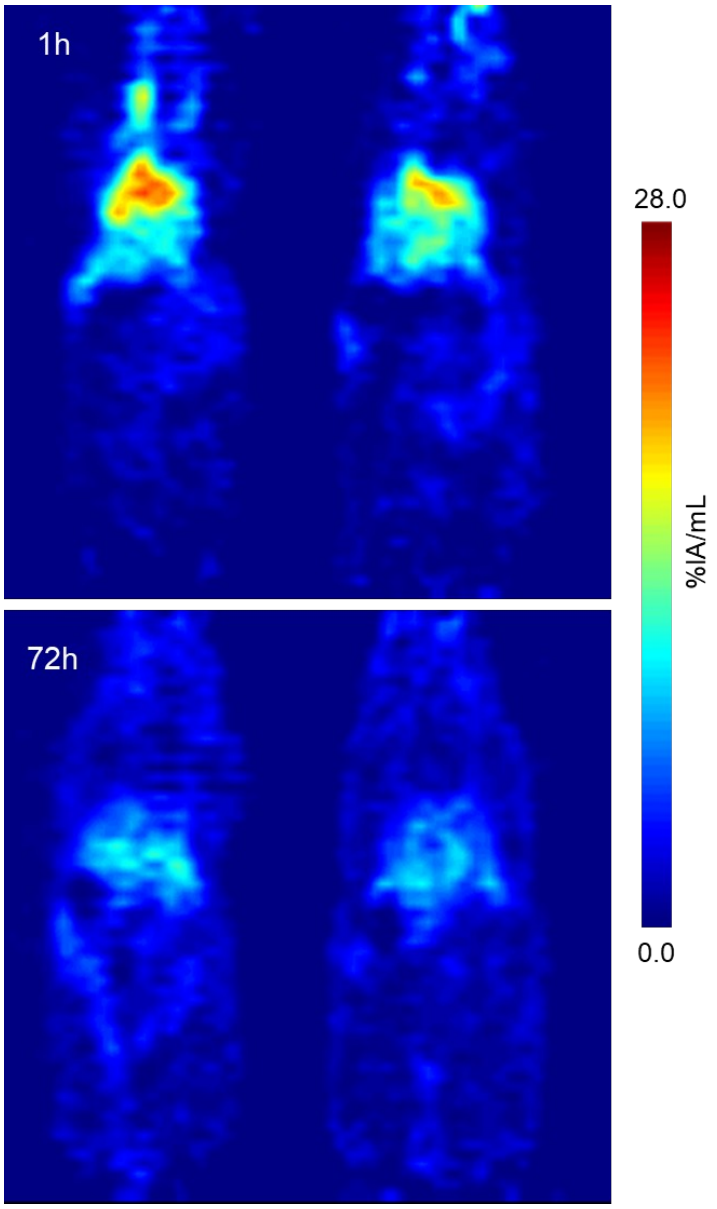

Figure 14. *In vivo* positron emission tomography (PET) images of [^{89}Zr][Zr(opdivo-py$_2$-macrodipa)] at 1 and 72 h following retro-orbital injection in naïve ND4 mice, coronal view of the mice. No activity accumulation in the bone was observed over time indicating *in vivo* stability of the radio conjugate

To further support the PET findings, *ex vivo* biodistribution studies were conducted over a 72 h period. Corroborating imaging findings, we report high early blood pool and organ activity with minimal and non-increasing bone uptake (**Figure 15**, **Table S9**), confirming high *in vivo* stability.

The radioconjugate [^{225}Ac][Ac(opdivo-py$_2$-macrodipa-sq)] exhibited elevated initial activity in the blood pool and major organs. Although early organ uptake was relatively high, the radiotracer was efficiently cleared from most tissues by days 4 and 6 post-administration (**Figure 15**, **Table S10**). Notably, bone uptake remained low throughout the study, indicating high *in vivo* stability of the conjugate.

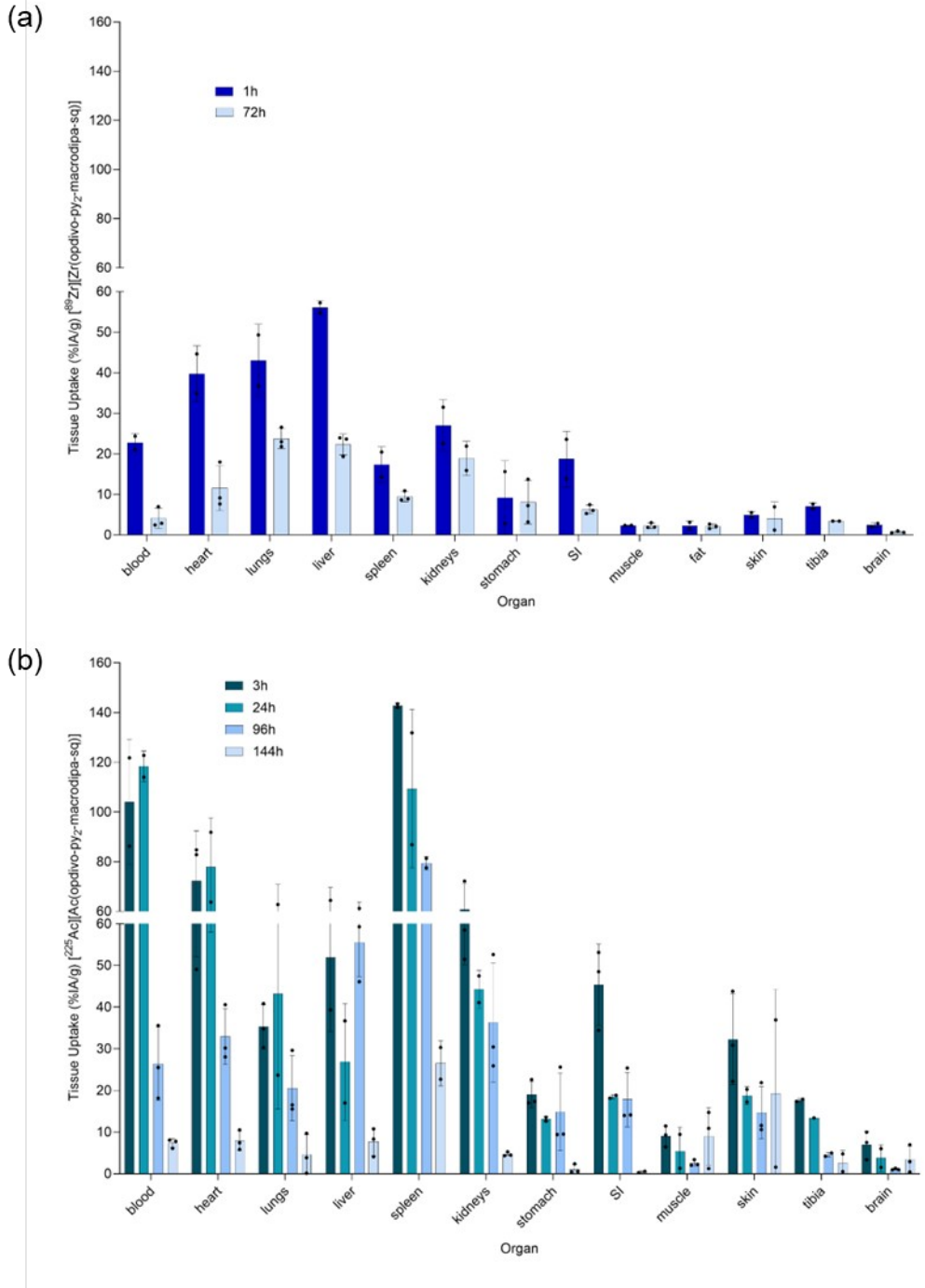

Figure 15. Organ distribution of (a) [^{89}Zr][Zr(opdivo-py$_2$-macrodipa-sq)] and (b) [^{225}Ac][Ac(opdivo-py$_2$-macrodipa-sq)] following retro-orbital injection in naïve mice; Values for each time point are given as %IA/g; %IA/g = percent injected activity per g of tissue; SI = small intestine. Both conjugates exhibited similar distribution profiles, efficient systemic clearance of activity over time and consistently low bone uptake, indicating *in vivo* stability.

Discussion

Radiopharmaceutical therapy is a rapidly growing field that offers targeted treatment options for disseminated cancers. Theranostic approaches enable personalized treatment and monitor therapeutic response in real time by linking diagnostic imaging with therapeutic radionuclide distribution. Although this modality holds great promise, key concerns include off-target toxicity and questions of quantitative accuracy of imaging techniques [4].

Ac-225 is an attractive alpha-emitter for targeted alpha therapy (TAT) due to its 9.92-day half-life and the emission of four high energy α-particles during its decay chain. The half-life is particularly well suited to antibody-based radiopharmaceuticals with slower pharmacokinetics while remaining compatible with peptide-based targeting vectors, including PSMA- and somatostatin receptor-targeted agents. [41,42] DOTA is the conventional chelator for the largest trivalent metal ion ^{225}Ac. However, DOTA's inverse thermodynamic stability with metal ion size precludes stable chelation of small ionic radii PET emitters with sufficient half-life for later phase imaging has been a challenge. The macrocyclic chelator macropa has been developed for coordinating large ionic radius metal ions such as [^{225}Ac]Ac^{3+}; however, the cavity size and donor arrangement of this 18-membered ring are poorly matched to high charge-density, small ionic radii radionuclides.

For PET imaging, ^{89}Zr is preferred for late-phase imaging of antibodies and proteins due to its favorable emission properties, availability, and long half-life. We evaluated the coordination efficiency, radiolabeling, and stability of py$_2$-macrodipa with [^{89}Zr]Zr^{4+} and [^{225}Ac]Ac^{3+}. Both radionuclides exhibited efficient complexation and high radiochemical yields. Quantitative [^{89}Zr]Zr^{4+} labeling was performed at 90 °C (oxalic acid precursor), whereas [^{225}Ac]Ac^{3+} binding proceeded under mild, room-temperature conditions. Pandya et al. reported exceptional thermodynamic stability of ^{89}Zr-DOTA relative to DFO. However, quantitative labeling required high temperatures, limiting applicability to protein conjugates. In contrast, py$_2$-macrodipa achieved 40% RCY with [^{89}Zr]Zr^{4+} at 37 °C,

whereas DOTA showed no detectable ^{89}Zr incorporation under identical conditions, recapitulating prior findings [43].

Recent studies demonstrated that effective DOTA labeling requires the ^{89}Zr precursor to be in the form of [^{89}Zr]$ZrCl_4$ rather than [^{89}Zr]Zr^{4+} in oxalic acid [22,44,45]. Quantitative radiolabeling of 9-membered NOTA and 12-membered PCTA chelators using [^{89}Zr]$ZrCl_4$ at 37 ˚C were achieved, while 13-membered TRITA required microwave heating and 14-membered TETA showed poor RCY even with such assistance [45]. Collectively, these findings indicate that increasing coordination environment size of the ligands weakens the metal-ligand bonding interaction.

The oxalate anion forms a stable [^{89}Zr]Zr complex in aqueous media, thermodynamically preventing trans-chelation by DOTA In contrast, [^{89}Zr]$ZrCl_4$ rapidly hydrolyzes to form hydroxo- and oxo-bridged compounds that are susceptible to trans-chelation by tetraazamacrocycle ligand DOTA [46]. Based on these properties, we investigated labeling the dual-size selective chelator with [^{89}Zr]$ZrCl_4$. Surprisingly, both macropa and py_2-macrodipa failed to incorporate [^{89}Zr]Zr^{4+} at 25 ˚C, nor at elevated temperature. Notably, labeling of [^{89}Zr]Zr^{4+} with DFO and DOTA was achieved 25 ˚C and 90 ˚C respectively with [^{89}Zr]$ZrCl_4$ as previously reported. Trace metal contamination may be a factor for our results [44] and the distinctive selectivity of py_2-macrodipa ligand for the oxalic form of the radioisotope will be investigated further for future ligand development.

The [^{89}Zr][Zr(py_2-macrodipa)]$^{2+}$ complex showed a high degree of *in vitro* stability in human serum; greater than 95% remained intact after 48 h. This was similar to the conventional DFO-complex. As expected, the kinetic inertness of [^{225}Ac][Ac(py_2-macrodipa)]$^{+}$ in human serum was also validated. By contrast, macrocyclic macropa chelator showed efficient *in vitro* stability for [^{225}Ac]Ac^{3+} but was not compatible for [^{89}Zr]Zr^{4+}

We next explored the *in vivo* stability of the complexes, using both PET imaging and acute biodistribution studies. The dual size selective chelator py_2-macrodipa displayed robust *in vivo* stability for both radionulcides. Longitudinal PET acquisitions revealed alternative excretion pathways for DFO and py_2-macrodipa ligands with Zr-89. The majority of the injected activity of py_2-macrodipa complex was observed in the intestine which was excreted over the course of the experiment. The DFO-complex showed rapid renal excretion. Notably, both complexes showed minimal bone uptake, indicating no release of free [^{89}Zr]Zr^{4+} ion from the ligand *in vivo*. Despite this difference, both complexes showed low uptake in other organs and neither complex presented substantial accumulation over time. The amount of activity in the bone for py_2-macrodipa complex is higher than that of

DFO-complex; this could be the result of the unchelated [^{89}Zr]Zr^{4+} cation as we injected [^{89}Zr][Zr(py_2-macrodipa)]$^{2+}$ complex with 87% purity (**Figure 5**). Radiochemical purity should not be a concern as the radiolabeled compound can be purified with a C18 cartridge (**Figure S12**). This observation can also be inferred from significant amount of activity detected in the bone for free [^{89}Zr]Zr^{4+} and the [^{89}Zr][Zr(macropa)]$^{2+}$ complex from biodistribution study. The biodistribution results of [^{225}Ac][Ac(py_2-macrodipa)]$^{+}$ complex revealed high degree of *in vivo* stability. Both [^{89}Zr][Zr(py_2-macrodipa)]$^{2+}$ and [^{225}Ac][Ac(py_2-macrodipa)]$^{+}$ complexes demonstrated broadly similar activity clearance and kinetics, with some differences in organ-specific activity accumulation noted. The 24 h biodistribution study revealed substantial clearance and significant reduction in whole-body radioactivity for both complexes. The combination of *in vitro* and *in vivo* data addresses the stability of the py_2-macrodipa complexes. This motivates further development of a new bifunctional chelator py_2-macropdipa-sq by incorporating squaramide ethyl ester functional group with a PEG linker for antibody conjugation. Compared with isothiocyanates, the squaramide functional group is more stable, and reacts selectively with lysine residues on antibodies to form stable amide bonds. The py_2-macrodipa-sq-opdivo quantitatively incorporates both ^{89}Zr and ^{225}Ac isotopes using mild reaction condition. The resulting radioconjugates demonstrated high kinetic inertness when challenged in human serum.

Administration of [^{89}Zr][Zr(opdivo-py_2-macrodipa-sq)] in naïve mice revealed a high degree of *in vivo* stability, as assessed by PET imaging and biodistribution studies. PET images acquired at early time points (1 h post-injection) showed high heart uptake and moderate liver uptake, with circulation persisting up to 72 h and minimal skeletal accumulation. Biodistribution data corroborated these findings, with negligible bone uptake, further supporting the *in vivo* stability of the complex. The radioconjugate exhibited dual clearance pathways, undergoing both hepatobiliary and renal excretion. Although initial uptake of [^{225}Ac][Ac(opdivo-py_2-macrodipa-sq)] in blood pool and major organs was relatively high compared to ^{89}Zr-conjugate, both radioconjugates exhibited minimal bone accumulation. The biodistribution study showed accumulation of activity in all blood rich organs including the liver and kidneys, indicating the involvement of both hepatobiliary and renal excretion pathways. After validating the *in vivo* stability of the radioconjugates, the pharmacokinetics of ^{225}Ac- and ^{89}Zr-Opdivo-py_2-macrodipa-sq were found to be similar (**Figure 15**). The observed differences in activity biodistribution may result from the administration of different antibody masses (8 and 22 µg of antibody for ^{89}Zr and ^{225}Ac, respectively), which can influence target saturation, tissue distribution, and clearance kinetics. Importantly, despite these early differences, both radioconjugates exhibited efficient systemic clearance over time and consistently low bone uptake,

indicating neither *in vivo* demetallation nor radiolabel instability. In contrast to free [^{225}Ac]Ac^{3+} ion, which predominantly accumulates in bone and liver over time, activity associated with the ^{225}Ac-radioconjugate was largely cleared from these tissues by days 4 and 6 post-administration. Similarly, ^{89}Zr-radioconjugate demonstrated no evidence of long-term accumulation in the bone underlines the *in vivo* stability.

Conclusions

In this report, we demonstrate the stable coordination of metal ions with distinct coordination characteristics, [^{89}Zr]Zr^{4+}, exhibiting high charge density and a preference for lower coordination numbers, and [^{225}Ac]Ac^{3+}, characterized by lower charge density and a tendency toward higher coordination numbers using the dual size-selective chelator py$_2$-macrodipa. The coordination chemistry of py$_2$-macrodipa with [^{89}Zr]Zr^{4+} was characterized by NMR spectroscopy, indicating formation of an asymmetric conformation. The crystal structure obtained for the [Zr(py-macrodipa)(OMe)]$^{+}$ complex provides additional evidence supporting the presence of Conformation B in this class of chelators. Both [^{89}Zr][Zr(py$_2$-macrodipa)]$^{2+}$ and [^{225}Ac][Ac(py$_2$-macrodipa)]$^{+}$ complexes displayed robust stability both *in vitro* in human serum and *in vivo* in mice. PET imaging and biodistribution study showed rapid clearance of injected activity for [^{89}Zr][Zr(py$_2$-macrodipa)]$^{2+}$ complex without accumulating in the organs over time. Notably, its coordination with [^{225}Ac]Ac^{3+} also revealed good biological behavior, rapid clearance and absence of demetallation. In addition, both complexes exhibited similar activity distribution and excretion profiles. These results support the development of py$_2$-macrodipa-sq as a bifunctional chelator for antibody conjugation. The squaramide modification enables stable, selective lysine conjugation and efficient incorporation of both ^{89}Zr and ^{225}Ac under mild conditions. Radioconjugates showed high kinetic inertness in serum and strong resistance to demetallation *in vivo*, with minimal bone accumulation and favorable clearance profiles, highlighting their potential for effective ^{225}Ac/^{89}Zr theranostic applications. Evaluation of py$_2$-macrodipa-based radioconjugates in tumor-bearing mouse models will include side-by-side comparison of ^{89}Zr- and ^{225}Ac-labeled constructs under identical conditions to assess theranostic potential, as well as the identification of improved radionuclide pairings to further enhance the theranostic potential of this chelator system.

Experimental Section

Materials and Methods

The experimental data supporting this article is provided in the ESI. The X-ray crystallographic data is deposited in the Cambridge Structural Database (CCDC) as crystallographic information files (cif) under deposition number 2430371.

Preparation of Complexes for NMR Spectroscopic Analysis

NMR samples of py-macrodipa and py_2-macrodipa complexes with Zr^{4+} were prepared in H_2O. Ligand stock solutions (2 mM) were prepared in H_2O. Metal stock solutions (2 mM) were prepared by dissolving $Zr(acac)_4$ in H_2O immediately prior to use. Complex solutions were obtained by mixing 1.0 mL of ligand stock with 1.0 mL of the corresponding metal stock to afford final concentrations of 1.0 mM ligand and 1.0 mM metal (1:1 M:L ratio). The pH of the solution was adjusted to 5.0 using 1 M NaOH, and the mixture was stirred at room temperature overnight. The resulting solutions were lyophilized to dryness. The obtained solids were subsequently redissolved in D_2O for NMR analysis.

Single Crystal Growth of Zr(py-macrodipa)(OMe)][Cl] DMF

The ligand py-macrodipa·3HCl·3.5H_2O (24.6 mg, 0.033 mmol) was dissolved in methanol (MeOH, 400 µL), and Triethylamine (Et_3N, 22.9 µL, 0.165 mmol) was added. A solution of $Zr(acac)_4$ (17.6 mg, 0.036 mmol) in MeOH (400 µL) was added dropwise to the ligand solution. This reaction mixture was then stirred for 48 h at room temperature (RT). Afterwards, the reaction mixture was transferred into a scintillation vial, and air-dried overnight in the fume hood, affording a white solid (44.2 mg). Slow diffusion of Diethyl ether (Et_2O) into a Dimethylformamide (DMF) solution of this material afforded X-ray quality crystals of [Zr(py-macrodipa)(OMe)][Cl] DMF.

Low-temperature X-ray diffraction data were collected on a Rigaku XtaLAB Synergy diffractometer coupled to a Rigaku Hypix detector with Cu Kα radiation (λ = 1.54184 Å), from a PhotonJet micro-focus X-ray source at 100 K. The diffraction images were processed and scaled using the CrysAlisPro software. The structures were solved through intrinsic phasing using SHELXT [47] and refined against F2 on all data by full-matrix least squares with SHELXL following established refinement strategies [48,49]. All non-hydrogen atoms were refined anisotropically. All hydrogen atoms bound to carbon were included in the model at geometrically calculated positions and refined using a riding model. Hydrogen atoms bound to oxygen were located in the difference Fourier synthesis and subsequently refined semi-freely with the help of distance restraints. The isotropic displacement parameters of all hydrogen atoms were fixed to 1.2 times the Ueq value of the atoms they are linked to (1.5 times for methyl groups). The X-ray crystallography data are presented in **Table S11**.

.

Synthesis of methyl 6-(3,13-dioxa-6,10-diaza-1,8(2,6)-dipyridinacyclotetradecaphane-6-ylmethyl)picolinate (3)

To a solution of 3,13-dioxa-6,10-diaza-1,8(2,6)-dipyridinacyclotetradecaphane ((**1**),150 mg, 0.46 mmol) in anhydrous MeCN (100 mL) was added Na_2CO_3 (145.2 mg, 1.37 mmol). The reaction mixture was heated to reflux for 2 h and then allowed to cool to room temperature. A solution of methyl 6-(bromomethyl)picolinate ((**2**), 63.1 mg, 0.274 mmol) in anhydrous MeCN (100 mL) was added dropwise over 1 h, and the resulting mixture was heated to reflux overnight. After cooling to room temperature, the mixture was filtered, and the filtrate was concentrated under reduced pressure to afford a yellow oil. The crude product was dissolved in H_2O (2 mL, 0.1% TFA) and purified by preparative HPLC (method described above) to give the desired product as a white solid (108 mg, 49.5%). ^{1}H NMR (500 MHz, DMSO-d_6) δ 7.56 (d, J = 7.3 2.3 Hz, 4H), 7.55 - 7.43 (m, 2H), 7.39 - 7.12 (m, 3H), 4.40 (s, 4H), 4.00 (s, 4H), 3.39 (s, 4H), 3.01 (s, 2H), 2.33 (s, 2H). ESI-MS m/z: 239.6; calcd for $[C_{26}H_{31}N_5O_4 + 2H]^{2+}$: 239.6.

Synthesis of 6-((10-((6-carboxypyridin-2-yl)methyl)-3,13-dioxa-6,10-diaza-1,8(2,6)-dipyridinacyclotetradecaphane-6-yl)methyl)-4-(prop-2-yn-1-yloxy)picolinic acid (5)

To a solution of **3** (100 mg, 0.21 mmol) in anhydrous MeCN (10 mL) was added Na_2CO_3 (66.6 mg, 0.63 mmol), and the reaction mixture was heated to reflux for 2 h. Methyl 6-(bromomethyl)-4-(prop-2-yn-1-yloxy)picolinate ((**4**), 29.8 mg, 0.10 mmol) was then added, and the resulting mixture was heated to reflux overnight. After cooling to room temperature, the mixture was filtered, and the filtrate was concentrated under reduced pressure to afford a yellow oil. The crude product was dissolved in MeOH (5 mL), and LiOH (31.9 mg, 1.33 mmol) was added. The resulting solution was stirred at room temperature overnight, then concentrated under reduced pressure to afford a yellow oil. The crude material was dissolved in H_2O (2 mL, 0.1% TFA) and purified by preparative HPLC (method described above) to give the desired product as a white solid (72.4 mg, 53%). ^{1}H NMR (400 MHz, MeOD) δ 8.20 (d, J = 7.7 Hz, 8H), 8.12 (m, 3H), 7.81 (d, J = 2.2 Hz, 2H), 7.74 (d, J = 7.7 Hz, 2H), 7.44 (s, 2H), 4.80 (s, 2H), 4.73 (s, 2H), 4.60 (t, J = 4.9 Hz, 4H), 3.96 (d, J = 6.2 Hz, 4H), 3.93 (s, 1H), 3.85 (d, J = 4.9 Hz, 4H), 2.50 (t, J = 6.0 Hz, 4H). ESI-MS m/z: 327.9; calcd for $[C_{35}H_{36}N_6O_7 + 2H]^{2+}$: 327.2.

Synthesis of 6-((10-((6-carboxypyridin-2-yl)methyl)-3,13-dioxa-6,10-diaza-1,8(2,6)-dipyridinacyclotetradecaphane-6-yl)methyl)-4-((1-(2-(2-(2-((2-ethoxy-3,4-dioxocyclobut-1-en-1-yl)amino)ethoxy)ethoxy)ethyl)-1*H*-1,2,3-triazol-4-yl)methoxy)picolinic acid (7)

$CuSO_4$ (2.2 mg, 0.014 mmol) and sodium ascorbate (6.4 mg, 0.032 mmol) were dissolved in H_2O (5 mL) to generate the Cu(I) species in situ. TBTA (28 mg, 0.057 mmol) was added, followed by 3-((2-(2-(2-azidoethoxy)ethoxy)ethyl)amino)-4-ethoxycyclobut-3-ene-1,2-dione ((**6**), 18.9 mg, 0.63 mmol), and the mixture was stirred for 10 min. Compound **5**

(41.1 mg, 0.63 mmol) was then added, and the reaction mixture was purged with N_2 for 15 min. Reaction progress was monitored by LC-MS, confirming complete consumption of azide species. After 1 h, Na_2EDTA (26 mg, 0.07 mmol) was added to chelate residual copper. The pale green solution was concentrated to dryness under reduced pressure and dried in vacuo. The crude material was purified by preparative HPLC (method described above); the combined fractions were lyophilized to afford an off-white powder (54.2 mg, 88%).^{1}H NMR (500 MHz, MeOD) δ 7.96 (dd, *J* = 7.7, 1.1 Hz, 2H), 7.85 (t, *J* = 7.8 Hz, 2H), 7.71 - 7.62 (m, 3H), 7.34 (d, *J* = 8.4 Hz, 2H), 7.21 (dd, *J* = 15.0, 8.1 Hz, 2H), 6.81 (s, 1H), 4.56 (d, *J* = 14.4 Hz, 8H), 4.18 (t, *J* = 6.6 Hz, 8H), 3.90 (s, 3H), 3.81 (s, 4H), 3.75 (s, 4H), 3.63 (s, 4H), 3.07 - 2.96 (m, 4H), 2.81 (t, *J* = 5.4 Hz, 4H) ESI-MS m/z: 478.2; calcd for $[C_{48}H_{54}N_{10}O_{12} + 2H]^{2+}$: 478.8.

Radiolabeling of DFO, macropa and py_2-macrodipa with Zr-89 and Ac-225

DFO, macropa and py_2-macrodipa were dissolved in chelex-water to prepare 15 mM stock solutions. From these stock solutions, serial dilutions were performed to prepare ligand solutions at varying concentrations (10^{-3}-10^{-12} M). For the labeling studies, the pH of the $[^{89}Zr]Zr^{4+}$ in 1 M oxalic acid was adjusted to 6.0-6.5 with 0.1M sodium carbonate (Na_2CO_3). A 20 µL aliquot of each ligand solution was further diluted with 50 µL 0.5M HEPES buffer (pH 6.5). Subsequently, 4 µL (0.2 MBq) of balanced $[^{89}Zr]Zr^{4+}$ was added. The mixture was vortexed and incubated at either 37 ˚C or 90 ˚C for 30 min. Radiochemical yield was evaluated using iTLC-SG with 50 mM EDTA pH 5.5 running buffer. Radiolabeled complex remained at the origin line (Rf = 0), while free $[^{89}Zr]Zr^{4+}$ migrated with the solvent front (Rf ≈ 1). After incubation, approximately 2 µL aliquots were spotted on iTLC-SG plates and developed. Radiochemical yields (RCY) were measured using gas proportional scanner (Bioscan AR-2000).

For the radiolabeling of $[^{89}Zr]Zr^{4+}$ in 1 M HCl solution, DFO, DOTA, and py_2-macrodipa were initially dissolved in 0.1 M HEPES buffer (pH 6.5) to create 100 mM stock solutions. From these stock solutions, serial dilutions were performed to prepare ligand solutions at varying concentrations. A 5 µL aliquot of each ligand solution was further diluted with 43 µL of 0.1 M HEPES buffer (pH 6.5) and 2 µL of $[^{89}Zr]ZrCl_4$ solution in 1 M HCl (1.85 MBq) was added to the mixture. This combination was incubated at either 25 °C or 90 °C for 1 hour. Radiochemical yields were determined using the previously described method for labeling $[^{89}Zr]Zr^{4+}$ in oxalic acid.

For $[^{225}Ac]Ac^{3+}$ labeling with macropa and py_2-macrodipa, dry $[^{225}Ac]Ac(NO_3)_3$ (2.96 MBq) source received was diluted with 0.05M HCl (200 µL). The pH of $[^{225}Ac]Ac^{3+}$ solution (20 µL, 0.2MBq) was adjusted to 6.0 with 0.5M ammonium acetate (NH_4OAc) buffer (200 µL, pH 6.0). Afterwards, macropa ligand (100 µL, 15mM) was added to it and the mixture was

incubated at room temperature for 15min. Similar radiolabeling protocol was followed for py_2-macrodipa ligand. Radiochemical yield (>96%) was determined with radio-TLC.

Antibody Conjugation

Conjugation of the py_2-macrodipa-sq to Opdivo antibody was performed using a chelator to antibody ratio of 20:1. Before conjugation buffer was exchanged by spin desalting column (Zeba, 40kDa, 0.5mL, Thermo Scientific) to Sodium bicarbonate buffer (0.5 M, pH 8.5-9.0). The mixture of Opdivo and the chelator was incubated in 0.5 M sodium bicarbonate buffer (pH 8.5-9.0) at 37 ˚C for overnight. Before radiolabeling with Ac-225 and Zr-89, buffer was exchanged into 0.5 M ammonium acetate (NH_4OAc, pH 6.5) and 0.5 M 4-(2-hydroxyethyl)-1-piperazineethanesulfonic acid (HEPES. pH 7.0) respectively with a zeba column (40kDa, 0.5mL). The purity of the antibody conjugate was measured by FPLC using an Enrich SEC 650 (10×300) column.

Radiolabeling with ^{89}Zr and ^{225}Ac isotopes

For the labeling studies, the pH of the $[^{89}Zr]Zr^{4+}$ in 1M oxalic acid was adjusted to 7.0 with 0.5M sodium carbonate (Na_2CO_3). Neutralized $[^{89}Zr]Zr^{4+}$ (33 Mbq) was reacted with the antibody conjugate (200µg) in 0.5 M HEPES buffer (pH 7) at 37˚C for 2h. For Ac-225 labeling study, dry $[^{225}Ac]Ac(NO_3)_3$ source received was diluted with 0.05 M HCl (15 µL). The pH of $[^{225}Ac]Ac^{3+}$ solution (15 µL, 1.04 MBq) was adjusted to 6.0 with 0.5 M ammonium acetate (NH_4OAc) buffer (200 µL, pH 6.0). Afterwards, the conjugate (100 µg) in 0.5M ammonium acetate buffe was added to it and the mixture was incubated at room temperature for 1h. Ethylenediaminetetraacetic acid (EDTA,10µL, 50 mM pH 6.0) was added to each reaction mixture, then the radioconjugate was purified in saline using a preconditioned spin desalting column (40 kDa, 2mL). The radiochemical yield and purity (RCY and RCP) were verified (**Figure 13**) by radio-TLC (Bioscan AR-2000). Free metals migrated with the solvent front (50mM EDTA mobile phase, Rf=1), whereas the labeled antibodies remained at the baseline (Rf ~ 0).

Human Serum Stability

The complexes were prepared with the radiolabeling protocol as described above for the serum stability study. A starting 20µL (25.16 MBq) of balanced $[^{89}Zr]Zr^{4+}$ (pH 6.5-7.0 with 0.1 M Na_2CO_3) was diluted with 150 µL 0.5 M HEPES buffer (pH 6.5) and 100 µL 15 mM each ligand (DFO, macropa and py_2-macrodipa) was added. The reaction mixtures were incubated at either 37 ˚C (for DFO ligand) or 90 ˚C for 30 min. Radiochemical yield was determined to be 99, 87 and 86% respectively for ^{89}Zr-complexes with DFO, py_2-macrodipa and macropa. Both $[^{89}Zr][Zr(py_2\text{-macrodipa})]^{2+}$ and $[^{89}Zr][Zr(macropa)]^{2+}$ compounds were further purified using C18 cartridge with methanol/acetonitrile (and 0.1%

TFA) solvent mixture. The solvent was evaporated to dryness to give final activity 3.7-4.4 MBq; activity was further diluted with 100 µL normal saline.

To assess stability with a protein challenge, 20µL of each radiolabeled compound (0.74-1.85 MBq) was incubated in human serum (purchased from Sigma, 400µL) at 37 ˚C, under gentle shaking over 48 h. At predetermined time points, the stability was measured by radio-TLC (**Figure S17**), and the %intact complex values were shown in **Table S4**. ^{225}Ac][Ac(py$_2$-macrodipa)]$^+$ and [^{225}Ac][Ac(macropa)]$^+$ complexes were synthesized as described above. To assess stability of the actinium ligands, we used 10 µL each compound (0.01 MBq) incubated in human serum (400 µL) at 37 ˚C. Serum stability was monitored (at 5 min, 1, 4, 24, 48, 72 and 144 h) with iTLC-SG using 50mM EDTA (pH5.5) as mobile phase (**Figure S16, S18** and **Table S5**).

The [^{225}Ac][Ac(opdivo-py$_2$-macrodipa-sq)] radioconjugate was prepared with the radiolabeling protocol as described above for serum stability study. ^{225}Ac-radioconstruct (15µg/0.07MBq) was incubated in human serum (400 µL) at 37 ˚C, under gentle shaking over 5 days. The stability was measured by radio-TLC (**Figure S22**), and the %-intact complex values were shown in **Table S7**

[^{89}Zr][Zr(opdivo-py$_2$-macrodipa-sq)] construct was synthesized as described above (radiolabeling section) and challenged (~30 µg/0.93 MBq) in human serum (400 µL). The radioconjugate with a RCP >85% was incubated at 37 ˚C, under gentle shaking over 48 h and the kinetic inertness was monitored by radio-TLC (**Figure S23**, **Table S6**).

Biodistribution Study of ^{89}Zr and ^{225}Ac-labeled complexes

For preparation of [^{89}Zr][Zr(py$_2$-macrodipa)]$^{2+}$ 30 µL of (18.5 MBq) balanced [^{89}Zr]Zr^{4+} in 0.1M oxalic acid (pH was adjusted to 6.5-7.0 with 0.1M Na_2CO_3) solution was added to HEPES buffer (100 µL, 0.5 M, pH 6.5) to further adjust the pH to 6.5, and then 100 µL of 15 mM of py$_2$-macrodipa chelator was added to it. The mixture was vortexed and incubated at 90 ˚C for 30 min. Radiochemical yield was evaluated using iTLC-SG with a 50 mM EDTA pH 5.5 mobile phase. Radio-TLC was developed using a gas proportional scanner (Bioscan AR-2000) with a 1 min acquisition time. For subsequent *in vivo* evaluation, the labeled material was then diluted with 1.0 mL of normal saline (0.9% NaCl in deionized H_2O; Hospira), and activities were prepared in 30G syringes for administration. [^{89}Zr][Zr(macropa)]$^{2+}$ and [^{89}Zr][Zr(DFO)] were also prepared following the labeling conditions as described above in the radiolabeling section. Naive Swiss Webster female mice from (4 months; Charles River), were injected *via* the retroorbital with 100 µL, 2.04 - 4.3 MBq of each respective complex ([^{89}Zr][Zr(py$_2$-macrodipa)]$^{2+}$, [^{89}Zr][Zr(macropa)]$^{2+}$, [^{89}Zr][Zr(DFO)] and free [^{89}Zr]Zr^{4+}). Similarly, a biodistribution study was also performed for [^{225}Ac][Ac(py$_2$-macrodipa)]$^+$ and [^{225}Ac][Ac(macropa)]$^+$. Each mouse was injected with an activity of 0.013-0.02 MBq (100µL).

The organ recovery was performed at three predetermined time points 1, 4 and 24h post injection. Animals were euthanized by CO_2 asphyxiation prior to tissue dissection. A blood sample was acquired, and the organs of interest were collected (heart, lungs, liver, kidneys, spleen, stomach, small intestine, large intestine, skin, muscle, fat, tibia, calvaria, brain, and bone-marrow), rinsed of excess blood, weighed, and measured by γ counting (Wizard2, PerkinElmer). Data were corrected for background and decay, and the activity of each tissue was normalized to an injection standard. The organ uptake values were calculated as percent of injected activity per gram of tissue (%IA g^{-1}).

PET Imaging of ^{89}Zr-labeled complexes

PET imaging of naive swiss webster females was performed using free [^{89}Zr]Zr^{4+}, and [^{89}Zr][Zr(DFO)], [^{89}Zr][Zr(macropa)]$^{2+}$, [^{89}Zr][Zr(py$_2$-macrodipa)]$^{2+}$ complexes at 1, 4 and 24 h post injection (R4 microPET, Siemens). Tracer administration was performed with the animal under anesthesia by retroorbital injection. The imaged mouse was centered in the field of view and maintained under 1-2% isoflurane anesthesia during PET imaging. The calibration factor of the PET scanner was determined with a mouse-sized phantom composed of a cylinder uniformly filled with an aqueous solution of ^{18}F with a known activity concentration. Acquisitions were recorded using an energy window of 350-700 keV and coincidence-timing window of 6 ns. PET image data were corrected for detector non-uniformity, deadtime, random coincidences and physical decay and images were reconstructed by an iterative 3D maximum a prior (MAP) algorithm.

The acquired PET images were analyzed using ASIPro software (Siemens). Volume of interest (VOI) analysis of the acquired images was performed using ASIPro software, and the observed value (%IA/mL) represents the mean radiotracer accumulation in the organs. The sequential radioactivity measurements (%IA/mL) were plotted over time post-administration.

PET Imaging and Biodistribution Study of ^{89}Zr and ^{225}Ac-Antibody Constructs

PET imaging (R4 microPET, Siemens) of naive ND4 mice (Inotiv)5-6months old was performed using [^{89}Zr][Zr(opdivo-py$_2$-macrodipa-sq)] construct (100 µL, 1.9-2.2 MBq) at 1 and 72 h after administration of activity. VOIs were defined and %IA/mL was determined (ASIPro).

Biodistribution study with naïve ND4 was performed with injecting intravenously (retro orbital sinus) both radioconjugates. The animals received 0.02 MBq- and 1.5-1.9 MBq of of Ac-225 and Zr-89 labeled antibody respectively. Each mouse was injected with 8 and 22µg of the ^{89}Zr- and ^{225}Ac-labeled construct. Mice were euthanized via CO_2 asphyxiation, after which organs were collected and quantified using γ-counting (Wizard2, PerkinElmer)

at 1 and 72 h for Zr-89-construct and 0-, 1-, 4-, and 6-days post injection ^{225}Ac analog. The organ uptake values were calculated as percent of injected activity per gram of tissue (%IA g^{-1}).

Statistical Analysis:

Data calculated using Microsoft Excel are expressed as mean ± SD. Student's unpaired t test (GraphPad Prism 9) was used to determine statistical significance. Differences with *p* values < 0.05 were considered to be statistically significant.

Supporting Information

The data supporting this article have been included as part of ESI. Supporting Information is available free of charge via the journal website.

Author Contributions

Experiments were performed by MC, KKL, AH, TK, AF, AH. MC, KKL, JJW and DLJT wrote, and all authors edited and contributed to the manuscript.

Acknowledgement

This work was supported in part by NIH R01CA229893, R01CA240711 and R21EB034882 (DLJT), as well as the National Institutes of Biomedical Imaging and Bioengineering of the National Institutes of Health under the award number R56 EB029259 (JJW).

Declarations

All radioactive material handling and animal experiments were conducted in compliance with institutional regulations and approved by Environmental Health and Safety Radioactive Materials at Washington University in St. Louis under protocol D16-00245 and Institutional Animal Care and Use Committee protocol #22-0023.

Conflict of Interest

The authors have no conflicts of interest.

References

(1) Herrmann, K.; Schwaiger, M.; Lewis, J. S.; Solomon, S. B.; McNeil, B. J.; Baumann, M.; Gambhir, S. S.; Hricak, H.; Weissleder, R. Radiotheranostics: A Roadmap for Future Development. *Lancet Oncol.* **2020**, *21* (3), e146–e156.

(2) Jadvar, H.; Chen, X.; Cai, W.; Mahmood, U. Radiotheranostics in Cancer Diagnosis and Management. *Radiology* **2018**, *286* (2), 388–400.
(3) Tran-Gia, J.; Salas-Ramirez, M.; Lassmann, M. What You See Is Not What You Get: On the Accuracy of Voxel-Based Dosimetry in Molecular Radiotherapy. *J. Nucl. Med.* **2020**, *61* (8), 1178–1186.
(4) Salerno, I.; Dunn, N.; White, H.; Miyazaki, W.; Jeziorski, K.; Silvestros, D.; Jha, A.; Laforest, R.; Akerele, M. I.; Thomas, M. A.; Thorek, D. L. J. Quantitative Comparison of SPECT and PET Performance for Clinical Theranostic Applications. *J. Nucl. Med.* **2025**, jnumed.125.270987.
(5)Benabdallah N, Scheve W, Dunn N, Silvestros D, Schelker P, Abou D, Jammalamdaka U, Laforest R, Li Z, Liu J, Ballard DH, Maughan NM, Gay H, Baumann BC, Hobbs RF, Rogers B, Iravani A, Jha AK, Dehdashti F, Thorek DLJ. Practical Considerations for Quantitative Clinical SPECT/CT Imaging of Alpha Particle Emitting Radioisotopes. *Theranostics* **2021**, *11* (20), 9721–9737.
(6) Abou, D. S.; Rittenbach, A.; Tomlinson, R. E.; Finley, P. A.; Tsui, B.; Simons, B. W.; Jha, A. K.; Ulmert, D.; Riddle, R. C.; Thorek, D. L. J. Preclinical Single Photon Emission Computed Tomography of Alpha Particle-Emitting Radium-223. *Cancer Biother. Radiopharm.* **2020**. https://doi.org/10.1089/cbr.2019.3308.
(7) Li, Z.; Benabdallah, N.; Abou, D. S.; Baumann, B. C.; Dehdashti, F.; Ballard, D. H.; Liu, J.; Jammalamadaka, U.; Laforest, R. L.; Wahl, R. L.; Thorek, D. L. J.; Jha, A. K. A Projection-Domain Low-Count Quantitative SPECT Method for α-Particle-Emitting Radiopharmaceutical Therapy. *IEEE Trans. Radiat. Plasma Med. Sci.* **2023**, *7* (1), 62–74.
(8)Blake, P.; Johnson, B.; VanMeter, J. W. Positron Emission Tomography (PET) and Single Photon Emission Computed Tomography (SPECT): Clinical Applications. *J. Neuroophthalmol.* **2003**, *23* (1), 34–41.
(9) Phelps, M. E. PET: The Merging of Biology and Imaging into Molecular Imaging. *J. Nucl. Med.* **2000**, *41* (4), 661–681.
(10) van de Watering, F. C. J.; Rijpkema, M.; Perk, L.; Brinkmann, U.; Oyen, W. J. G.; Boerman, O. C. Zirconium-89 Labeled Antibodies: A New Tool for Molecular Imaging in Cancer Patients. *Biomed Res. Int.* **2014**, *2014*, 203601.
(11) van Loon, J.; Even, A. J. G.; Aerts, H. J. W. L.; Öllers, M.; Hoebers, F.; van Elmpt, W.; Dubois, L.; Dingemans, A.-M. C.; Lalisang, R. I.; Kempers, P.; Brans, B.; Winnepenninckx, V.; Speel, E.-J.; Thunnissen, E.; Smits, K. M.; Boellaard, R.; Vugts, D. J.; De Ruysscher, D.; Lambin, P. PET Imaging of Zirconium-89 Labelled Cetuximab: A Phase I Trial in Patients with Head and Neck and Lung Cancer. *Radiother. Oncol.* **2017**, *122* (2), 267–273.
(12) Ulaner, G. A.; Hyman, D. M.; Lyashchenko, S. K.; Lewis, J. S.; Carrasquillo, J. A. 89Zr-Trastuzumab PET/CT for Detection of Human Epidermal Growth Factor Receptor 2-Positive Metastases in Patients with Human Epidermal Growth Factor Receptor 2-Negative Primary Breast Cancer. *Clin. Nucl. Med.* **2017**, *42* (12), 912–917.

(13) Lindenberg, L.; Adler, S.; Turkbey, I. B.; Mertan, F.; Ton, A.; Do, K.; Kummar, S.; Gonzalez, E. M.; Bhattacharyya, S.; Jacobs, P. M.; Choyke, P. Dosimetry and First Human Experience with 89Zr-Panitumumab. *Am. J. Nucl. Med. Mol. Imaging* **2017**, *7* (4), 195–203.
(14) Jacobson, O.; Zhu, L.; Niu, G.; Weiss, I. D.; Szajek, L. P.; Ma, Y.; Sun, X.; Yan, Y.; Kiesewetter, D. O.; Liu, S.; Chen, X. MicroPET Imaging of Integrin Avβ3 Expressing Tumors Using 89Zr-RGD Peptides. *Mol. Imaging Biol.* **2011**, *13* (6), 1224–1233.
(15) Dietlein, F.; Kobe, C.; Vázquez, S. M.; Fischer, T.; Endepols, H.; Hohberg, M.; Reifegerst, M.; Neumaier, B.; Schomäcker, K.; Drzezga, A. E.; Dietlein, M. An 89Zr-Labeled PSMA Tracer for PET/CT Imaging of Prostate Cancer Patients. *J. Nucl. Med.* **2022**, *63* (4), 573–583.
(16) Basuli, F.; Vasalatiy, O.; Shi, J.; Lane, K. C.; Escorcia, F. E.; Swenson, R. E. Preparation of a Zirconium-89 Labeled Clickable DOTA Complex and Its Antibody Conjugate. *Pharmaceuticals (Basel)* **2024**, *17* (4). https://doi.org/10.3390/ph17040480.
(17) Babeker, H.; Njotu, F. N.; Pougoue Ketchemen, J.; Monzer, A.; Tikum, A. F.; Doroudi, A.; Nwangele, E.; Uppalapati, M.; Fonge, H. 225Ac/89Zr-Labeled N4MU01 Radioimmunoconjugates as Theranostics against Nectin-4-Positive Triple-Negative Breast Cancer. *J. Nucl. Med.* **2025**, *66* (4), 592–598.
(18) Nakata, N.; Kobashi, N.; Okumura, Y.; Sato, M.; Matono, M.; Otsuki, K.; Tanaka, A.; Hayashi, A. Radiation Dosimetry and Efficacy of an 89Zr/225Ac-Labeled Humanized Anti-MUC5AC Antibody. *Nucl. Med. Biol.* **2022**, *108–109*, 33–43.
(19) Zheng, L.; Yang, X.; Liu, J.; Wang, G.; Zhou, Z. A.; Xu, Y.; Gong, J.; Yang, J. Development of [89Zr]Zr-DFO-hu3F8 and [225Ac]Ac-DOTA-hu3F8 Theranostic Pairs Targeting GD2 in Neuroblastomas. *J. Med. Chem.* **2025**, *68* (23), 25607–25615.
(20) Vosjan, M. J. W. D.; Perk, L. R.; Visser, G. W. M.; Budde, M.; Jurek, P.; Kiefer, G. E.; van Dongen, G. A. M. S. Conjugation and Radiolabeling of Monoclonal Antibodies with Zirconium-89 for PET Imaging Using the Bifunctional Chelate p-Isothiocyanatobenzyl-Desferrioxamine. *Nat. Protoc.* **2010**, *5* (4), 739–743.
(21) Verel, I.; Visser, G. W. M.; Boellaard, R.; Stigter-van Walsum, M.; Snow, G. B.; van Dongen, G. A. M. S. 89Zr Immuno-PET: Comprehensive Procedures for the Production of 89Zr-Labeled Monoclonal Antibodies. *J. Nucl. Med.* **2003**, *44* (8), 1271–1281.
(22) Pandya, D. N.; Bhatt, N.; Yuan, H.; Day, C. S.; Ehrmann, B. M.; Wright, M.; Bierbach, U.; Wadas, T. J. Zirconium Tetraazamacrocycle Complexes Display Extraordinary Stability and Provide a New Strategy for Zirconium-89-Based Radiopharmaceutical Development. *Chem. Sci.* **2017**, *8* (3), 2309–2314.
(23) Kopp, I.; Cieslik, P.; Anger, K.; Josephy, T.; Neupert, L.; Velmurugan, G.; Gast, M.; Wadepohl, H.; Brühlmann, S. A.; Walther, M.; Kopka, K.; Bachmann, M.; Stephan, H.; Kubeil, M.; Comba, P. Bispidine Chelators for Radiopharmaceutical Applications with Lanthanide, Actinide, and Main Group Metal Ions. *Inorg. Chem.* **2023**, *62* (50), 20754–20768.

(24) Comba, P.; Jermilova, U.; Orvig, C.; Patrick, B. O.; Ramogida, C. F.; Rück, K.; Schneider, C.; Starke, M. Octadentate Picolinic Acid-Based Bispidine Ligand for Radiometal Ions. *Chemistry* **2017**, *23* (63), 15945–15956.
(25) Thiele, N. A.; Brown, V.; Kelly, J. M.; Amor-Coarasa, A.; Jermilova, U.; MacMillan, S. N.; Nikolopoulou, A.; Ponnala, S.; Ramogida, C. F.; Robertson, A. K. H.; Rodríguez-Rodríguez, C.; Schaffer, P.; Williams, C., Jr; Babich, J. W.; Radchenko, V.; Wilson, J. J. An Eighteen-Membered Macrocyclic Ligand for Actinium-225 Targeted Alpha Therapy. *Angew. Chem. Int. Ed Engl.* **2017**, *56* (46), 14712–14717.
(26) Abou, D. S.; Thiele, N. A.; Gutsche, N. T.; Villmer, A.; Zhang, H.; Woods, J. J.; Baidoo, K. E.; Escorcia, F. E.; Wilson, J. J.; Thorek, D. L. J. Towards the Stable Chelation of Radium for Biomedical Applications with an 18-Membered Macrocyclic Ligand. *Chem. Sci.* **2021**, *12* (10), 3733–3742.
(27) Hu, A.; Aluicio-Sarduy, E.; Brown, V.; MacMillan, S. N.; Becker, K. V.; Barnhart, T. E.; Radchenko, V.; Ramogida, C. F.; Engle, J. W.; Wilson, J. J. Py-Macrodipa: A Janus Chelator Capable of Binding Medicinally Relevant Rare-Earth Radiometals of Disparate Sizes. *J. Am. Chem. Soc.* **2021**, *143* (27), 10429–10440.
(28) Hu, A.; Brown, V.; MacMillan, S. N.; Radchenko, V.; Yang, H.; Wharton, L.; Ramogida, C. F.; Wilson, J. J. Chelating the Alpha Therapy Radionuclides 225Ac3+ and 213Bi3+ with 18-Membered Macrocyclic Ligands Macrodipa and Py-Macrodipa. *Inorg. Chem.* **2022**, *61* (2), 801–806.
(29) Hu, A.; MacMillan, S. N.; Wilson, J. J. Macrocyclic Ligands with an Unprecedented Size-Selectivity Pattern for the Lanthanide Ions. *J. Am. Chem. Soc.* **2020**, *142* (31), 13500–13506.
(30) Shannon, R. D. Revised Effective Ionic Radii and Systematic Studies of Interatomic Distances in Halides and Chalcogenides. *Acta Crystallogr. A* **1976**, *32* (5), 751–767.
(31) Zachariasen, W. H. Crystal Chemical Studies of the 5f-Series of Elements. I. New Structure Types. *Acta Crystallogr.* **1948**, *1* (5), 265–268.
(32) Deblonde, G. J.-P.; Zavarin, M.; Kersting, A. B. The Coordination Properties and Ionic Radius of Actinium: A 120-Year-Old Enigma. *Coord. Chem. Rev.* **2021**, *446* (214130), 214130.
(33) Fried, S.; Hagemann, F.; Zachariasen, W. H. The Preparation and Identification of Some Pure Actinium Compounds[1]. *J. Am. Chem. Soc.* **1950**, *72* (2), 771–775.
(34) Lundberg, D.; Persson, I. The Size of Actinoid(III) Ions – Structural Analysis vs. Common Misinterpretations. *Coord. Chem. Rev.* **2016**, *318*, 131–134.
(35) Hu, A.; Simms, M. E.; Kertesz, V.; Wilson, J. J.; Thiele, N. A. Chelating Rare-Earth Metals (Ln3+) and 225Ac3+ with the Dual-Size-Selective Macrocyclic Ligand Py2-Macrodipa. *Inorg. Chem.* **2022**, *61* (32), 12847–12855.
(36) Lee, K. K.; Chakraborty, M.; Hu, A.; Kanagasundaram, T.; Thorek, D. L. J.; Wilson, J. J. Chelation of [111In]In3+ with the Dual-Size-Selective Macrocycles Py-Macrodipa and Py2-Macrodipa. *Dalton Trans.* **2024**, *53* (35), 14634–14647.

(37) Rudd, S. E.; Roselt, P.; Cullinane, C.; Hicks, R. J.; Donnelly, P. S. A Desferrioxamine B Squaramide Ester for the Incorporation of Zirconium-89 into Antibodies. *Chem. Commun. (Camb.)* **2016**, *52* (80), 11889–11892.
(38) Kadassery, K. J.; King, A. P.; Fayn, S.; Baidoo, K. E.; MacMillan, S. N.; Escorcia, F. E.; Wilson, J. J. H2BZmacropa-NCS: A Bifunctional Chelator for Actinium-225 Targeted Alpha Therapy. *Bioconjug. Chem.* **2022**, *33* (6), 1222–1231.
(39) Hu, A.; Wilson, J. J. Advancing Chelation Strategies for Large Metal Ions for Nuclear Medicine Applications. *Acc. Chem. Res.* **2022**, *55* (6), 904–915.
(40) Morgan, K. A.; Wichmann, C. W.; Osellame, L. D.; Cao, Z.; Guo, N.; Scott, A. M.; Donnelly, P. S. Tumor Targeted Alpha Particle Therapy with an Actinium-225 Labelled Antibody for Carbonic Anhydrase IX. *Chem. Sci.* **2024**, *15* (9), 3372–3381.
(41) Shi, M.; Jakobsson, V.; Greifenstein, L.; Khong, P.-L.; Chen, X.; Baum, R. P.; Zhang, J. Alpha-Peptide Receptor Radionuclide Therapy Using Actinium-225 Labeled Somatostatin Receptor Agonists and Antagonists. *Front. Med. (Lausanne)* **2022**, *9*, 1034315.
(42) Zacherl, M. J.; Gildehaus, F. J.; Mittlmeier, L.; Böning, G.; Gosewisch, A.; Wenter, V.; Unterrainer, M.; Schmidt-Hegemann, N.; Belka, C.; Kretschmer, A.; Casuscelli, J.; Stief, C. G.; Unterrainer, M.; Bartenstein, P.; Todica, A.; Ilhan, H. First Clinical Results for PSMA-Targeted α-Therapy Using 225Ac-PSMA-I&T in Advanced-mCRPC Patients. *J. Nucl. Med.* **2021**, *62* (5), 669–674.
(43) Damerow, H.; Hübner, R.; Judmann, B.; Schirrmacher, R.; Wängler, B.; Fricker, G.; Wängler, C. Side-by-Side Comparison of Five Chelators for 89Zr-Labeling of Biomolecules: Investigation of Chemical/Radiochemical Properties and Complex Stability. *Cancers (Basel)* **2021**, *13* (24), 6349.
(44) Lyashchenko, S. K.; Tran, T.; Happel, S.; Park, H.; Bauer, D.; Jones, K.; Esposito, T. V.; Pillarsetty, N.; Lewis, J. S. [89Zr]ZrCl4 for Direct Radiolabeling of DOTA-Based Precursors. *Nucl. Med. Biol.* **2024**, *136–137* (108943), 108943.
(45) Pandya, D. N.; Henry, K. E.; Day, C. S.; Graves, S. A.; Nagle, V. L.; Dilling, T. R.; Sinha, A.; Ehrmann, B. M.; Bhatt, N. B.; Menda, Y.; Lewis, J. S.; Wadas, T. J. Polyazamacrocycle Ligands Facilitate 89Zr Radiochemistry and Yield 89Zr Complexes with Remarkable Stability. *Inorg. Chem.* **2020**, *59* (23), 17473–17487.
(46) Galeffi, B.; Simard, M.; Wuest, J. D. Coordination Chemistry of Zirconium Tetrachloride. Crystal Structure of the 1:2 Adduct with Pinacolone. *Inorg. Chem.* **1990**, *29* (5), 951–954.
(47) Sheldrick, G. M. SHELXT - Integrated Space-Group and Crystal-Structure Determination. *Acta Crystallogr. A Found. Adv.* **2015**, *71* (Pt 1), 3–8.
(48) Sheldrick, G. M. A Short History of SHELX. *Acta Crystallogr. A* **2008**, *64* (Pt 1), 112–122.
(49) Müller, P. Practical Suggestions for Better Crystal Structures. *Crystallogr. Rev.* **2009**, *15* (1), 57–83.

For Table of Contents Use Only

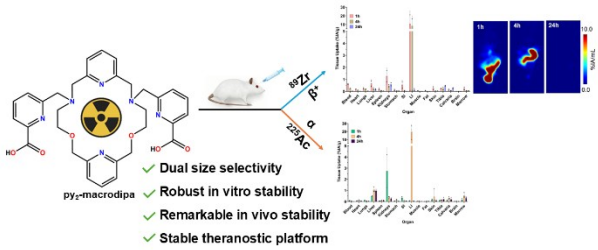
py2-macrodipa
89Zr
β+
α
225Ac
Dual size selectivity
Robust in vitro stability
Remarkable in vivo stability
Stable theranostic platform
1h
4h
24h

1